



Titanium oxynitride-supported Ru nanoparticles as exceptional electrocatalysts for alkaline hydrogen evolution reaction[☆]

M. Smiljanić^{a,*}, M. Bele^a, L. Pavko^a, A. Hrnjić^{a,b}, F. Ruiz-Zepeda^a, L. Bijelić^a,
A.R. Kamšek^{a,c}, M. Nuhanović^a, A. Marsel^a, L. Gašparič^{d,e}, A. Kokalj^{d,e},
N. Hodnik^{a,b,e,f,*}

^a Department of Materials Chemistry, National Institute of Chemistry, Hajdrihova 19, 1000 Ljubljana, Slovenia

^b University of Nova Gorica, Vipavska 13, 5000 Nova Gorica, Slovenia

^c Faculty of Chemistry and Chemical Engineering, University of Ljubljana, Večna pot 113, 1000 Ljubljana, Slovenia

^d Department of Physical and Organic Chemistry, Jožef Stefan Institute, Jamova cesta 39, 1000 Ljubljana, Slovenia

^e Jožef Stefan International Postgraduate School, Jamova cesta 39, 1000 Ljubljana, Slovenia

^f Department of Physics and Chemistry of Materials, Institute of Metals and Technology, Lepi pot 11, 1000 Ljubljana, Slovenia

ARTICLE INFO

Keywords:

Hydrogen evolution reaction
Alkaline electrolyte
Ruthenium
Titanium oxynitride
Metal-support interaction
DFT

ABSTRACT

We present a novel and highly efficient catalyst for the hydrogen evolution reaction (HER) consisting of low-loaded Ru nanoparticles dispersed on a titanium oxynitride-graphene oxide (Ru/TiON-C) support. Ru/TiON-C with a Ru loading of only 6 wt% is significantly more active for HER in alkaline media than the Ru/C analog. More importantly, Ru/TiON-C outperforms the Pt/C benchmark both intrinsically (2.5 times higher turnover frequency) and in terms of metal utilization (4.5 times higher mass activity). The exceptional HER activity of Ru/TiON-C is related to the metal-support interaction (MSI) induced by TiON, which was experimentally evidenced by X-ray photoelectron spectroscopy and further investigated by density functional theory calculations. It can be proposed that MSI enhances water dissociation properties and tunes hydrogen adsorption energy at Ru active sites, while stability is provided by the strong anchoring of the Ru nanoparticles on the TiON. The presented strategy to develop advanced electrocatalytic composites can be extended to other metallic active sites and electrochemical reactions.

1. Introduction

The increasing use of fossil fuels and the resulting emissions are worsening our environment, climate, and health. Due to its high energy density and complete environmental friendliness, hydrogen is a promising alternative to fossils as a primary energy carrier [1–3]. Water electrolysis is an electrochemical technology for carbon-free hydrogen production [4,5], which is obtained via the hydrogen evolution reaction (HER) at the cathode complemented by the counter-process of oxygen evolution at the anode. Platinum is considered the benchmark catalyst for HER [6], however, its high price and scarcity impede widespread usage. Therefore, developing active, durable, and affordable electrocatalysts for HER is an important and challenging task.

The initial step in HER is the formation of the adsorbed H atoms on the electrode surface in the so-called Volmer step. In acid media,

the Volmer step occurs readily due to the high availability of protons ($\text{H}^+ + \text{e}^- \rightarrow \text{H}^*$), and according to the Sabatier principle, the optimal HER catalysts should bind H-intermediates neither too strongly nor too weakly [7]. Gibbs energy for dissociative adsorption of hydrogen (ΔG_{H^*}) can be used as a descriptor for HER activity and correlated in the form of *Volcano plots* with experimentally measured activities [8–10]. Pt sits near the top of the Volcano curve thanks to close-to-optimal hydrogen adsorption energy, making Pt a nearly perfect HER catalyst [6]. It is thus very daunting to surpass the activity of Pt by simply designing Pt-free materials with better ΔG_{H^*} values. On the other hand, in alkaline media, an additional step of water dissociation is involved in the HER mechanism as the sources of the protons are water molecules ($\text{H}_2\text{O} + \text{e}^- \rightarrow \text{H}^* + \text{OH}^-$), which can be described by the energy barrier for water dissociation (E^{act}). The rate of HER on Pt in alkaline electrolytes is several orders of magnitude slower than in acid media due to sluggish

[☆] This article is part of a special issue entitled: 'Electrochemical Energy' published in Chemical Engineering Journal.

* Corresponding authors.

E-mail addresses: milutin.smiljanic@ki.si (M. Smiljanić), nejc.hodnik@ki.si (N. Hodnik).

<https://doi.org/10.1016/j.cej.2025.164204>

water activation [11], which opens up possibilities to develop efficient Pt-free catalysts by manipulating both ΔG_{H^*} and E^{act} parameters.

Ruthenium seems to be a good candidate for tailoring HER catalysts, as it combines the high activity and corrosion resistance of platinum group metals (PGM) with improved water dissociation properties [12,13]. In addition, Ru is the cheapest PGM member, with the average Ru price at around 25 % of the Pt price over the last ten years. However, Ru has a more negative ΔG_{H^*} value than Pt, i.e., Ru overbinds H atoms [14], and this issue needs to be addressed to develop competitive HER catalysts. Various strategies used to improve the activity of Ru are summarized in several recent review articles [12–15]. Alloying Ru with Cu was found to be beneficial for HER in alkaline and neutral media due to the ligand effect, which led to electronic rearrangements between Cu and Ru and modulated Ru–H* bonding and water activation properties [16]. Similar effects were also reported for the combination of Ru with Co [17], Ni [18], or Fe [19]. Doping with non-metals, such as phosphorus [20] or boron [21] can also enhance the HER performance of Ru. It was also shown that downsizing Ru nanoparticles to 2–3 nm (a few hundred atoms) increases the number of unsaturated atoms and defects [22,23]. Fabricating atomically dispersed Ru on suitable supports also resulted in excellent HER performances [24–26]. Another strategy reported to boost alkaline HER performance is to induce the growth of unexpected fcc-Ru nanostructures, which are typically not found in commercial Ru/C samples, where only thermodynamically favored hcp-Ru appears. Supporting Ru nanoparticles on graphitic carbon nitride complex with carbon (Ru/C₃N₄/C) led to a mixture of Ru fcc monophase, intergrown hcp/fcc phase, and hcp monophase [27]. The Ru/C₃N₄/C catalyst exhibited high activity for HER in alkaline media due to the reduced water dissociation barrier on anomalous Ru-fcc structures. Similar findings were also reported for fcc Ru nanodendrites [28] and fcc Ru nanorods epitaxially grown on Au nanowires [29].

In addition to metallic nanoparticles as active compounds, support materials are another essential part of electrocatalytic composites [30,31]. Certain supports have the ability to enhance the catalytic performance of active sites via metal–support interaction (MSI) [32,33]. MSI can induce charge redistribution between the support and nanoparticles, resulting in electronic interactions and thus changing the electrocatalytic activity of metallic sites. In the case of HER, MSI can be used to tune the ΔG_{H^*} and E^{act} descriptors of active sites. At the same time, the durability of nanocatalysts can be promoted by MSI by stronger anchoring between active metal nanoparticles and support, diminishing particle migration, coalescence, and detachment as the main HER degradation events [34,35]. For example, remarkable performance for alkaline HER was reported for Ru/WC_x catalyst, where WC_x provided rapid water dissociation, while subsequent hydrogen evolution took place on Ru-sites [36]. Similarly, Ru–MoO₂/C catalysts showed excellent HER activity due to the Ru–O–Mo bonding, which led to improved water dissociation and tuned Ru–H interaction [37]. Our group has recently introduced a nitrogen-doped titanium dioxide, also referred to as titanium oxynitride (TiON), as an advanced support for application in water splitting [38]. In the following studies, TiON was mixed with different carbon materials to improve its dispersion and increase the surface area [39]. These composites were initially tested as support for Ir nanoparticles for the oxygen evolution reaction, and significant performance enhancement was linked with MSI [38–41]. More recently, we have shown that supporting Pt nanoparticles on TiON improves their performance for HER [42] and oxygen reduction [43]. In the case of HER, MSI tuned the binding of chemisorbed H atoms on Pt sites, whereas strong anchoring promoted the stability.

This work demonstrates excellent HER properties of an electrocatalytic composite consisting of Ru nanoparticles supported on TiON dispersed over reduced graphene oxide (further denoted as Ru/TiON-C) with a low Ru loading of only 6 wt%. Characterization of Ru/TiON-C was performed using X-ray diffraction (XRD), scanning transmission electron microscopy (STEM), including 4D-STEM analyzed with unsupervised algorithms, and X-ray photoelectron spectroscopy (XPS).

Electrocatalytic HER tests conducted in an alkaline electrolyte revealed that the Ru/TiON-C composite is significantly more active than the Ru/C and Pt/C benchmarks. Moreover, Ru/TiON-C provided stable HER operation in both potentiodynamic and potentiostatic conditions. In acidic media, the Ru/TiON-C exhibited significantly higher HER activity than its Ru/C counterpart and approached the activity of the Pt/C reference. XPS analysis revealed the charge redistribution between TiON and Ru, which can be seen as experimental evidence of the MSI. DFT calculations showed stronger adhesion and confirmed more pronounced charge redistribution at the Ru/TiON interface compared to Ru/C. Therefore, the excellent HER performance of Ru/TiON-C can be attributed to the MSI, which influences both the hydrogen adsorption energy and the water dissociation barrier at Ru sites.

2. Experimental

2.1. Synthesis of Ru/TiON-C composite

In the first step of the synthesis of Ru/TiON-C composite, graphene oxide (GO) was synthesized. For the synthesis of GO, we used the slightly modified and improved Hummers method [44] in which a mixture of concentrated H₂SO₄/H₃PO₄ with volume ratio of 900 mL:100 mL was added to 20 g of graphite (Imerys, Timcal KS6L), and then KMnO₄ was added in aliquots (six aliquots of 20 g with stirring, resulting in a slight temperature rise to 35–40 °C). The reaction mixture was then stirred with a mechanical stirrer at room temperature in a 3-liter beaker for 10 days. The reaction mixture was then poured onto ice (1500 ml), and about 15 ml of 30 vol% H₂O₂ was added dropwise until the color changed from purple to yellow. The mixture was then transferred to 1 L plastic centrifuge bottles, diluted with ultrapure water, and centrifuged at 10,500 rpm for 30 min in a centrifuge (Sorvall LYNX 4000, Thermo Scientific). The supernatant was decanted, and the remaining solid was redispersed in a 5 vol% HCl ultrapure water solution for 2 h. The final purification step involved redispersing and soaking the suspension of GO in ultrapure water until the next day. The supernatant was then discarded by centrifugation at 10,500 rpm for 1 h. This final purification step was repeated a total of four times. After the last supernatant was discarded, GO was again dispersed in ultrapure water. In the case of GO, the suspension was treated with a homogenizer (Ultraturrax T-25 basic, IKA) for 1 h at maximum rpm to whip the product. Finally, the GO was freeze-dried. In the next step, the TiO₂ coating was prepared on GO. For this purpose, 0.1 g of the dried GO was mixed with 1 mL of propanol (Honeywell, 99.8 %) containing 1 mmol of Ti isopropoxide (Aldrich, 97 %). After mixing at room temperature, the Ti isopropoxide was hydrolyzed by adding 0.4 mL of water (Milli-Q water, 18.2 MΩ cm). The obtained mixture was then freeze-dried. In the third step, a 1.5 mL acetone solution containing 0.1 mmol RuCl₃·H₂O (Apollo Scientific) (1.5 mL) was added to the dried mixture and lightly ground in a mortar at 50 °C until evaporation. The mixture was then thermally treated in NH₃ with a flow of 100 ml/min. The temperature was first raised to 250 °C at a rate of 2 °C min^{−1} for 2 h, then to 750 °C at a rate of 10 °C min^{−1} for 9 h, and then cooled to room temperature at a rate of 10 °C min^{−1}. The same procedure was used to produce control samples consisting of Ru nanoparticles supported on TiON (without GO) and on GO (without TiON).

Ruthenium nanoparticles on carbon black were first prepared by dissolving 0.2 mmol RuCl₃·H₂O (Apollo Scientific) in 1 mL of water. Then, the obtained solution was mixed with 80 mg of Carbon Black (Vulcan XC72R, Cabot, USA) at 50 °C until evaporation by gentle grinding in a mortar. The resulting mixture was thermally treated in an ammonia atmosphere. The temperature was increased at a rate of 2 °C min^{−1} to 500 °C for 1 h and then cooled to room temperature at a rate of 10 °C min^{−1}.

The final Ru/TiON-C and homemade Ru/C materials contained 6 and 10 wt% of Ru, respectively, according to the ICP-OES analysis [45]. Commercial Pt/C, Ni/C (both 20 wt%), and RuO₂ catalysts used in this work were purchased from Premetek. The Pt/TiON-C catalyst used for

comparison was thoroughly characterized in our previous work [42].

2.2. Characterization of Ru/TiON-C

The obtained Ru/TiON-C composite was characterized by XRD, (S) TEM, and XPS. XRD pattern was recorded using a D4 Endeavor, Bruker AXS diffractometer with Cu-K α radiation ($\lambda = 1.5406 \text{ \AA}$), and a Sol-X energy-dispersive detector. For the detailed microstructural investigation, a Cs probe corrected scanning transmission electron microscope (Jeol ARM 200 CF) operated at 80 kV was used. 4D-STEM datasets were acquired using a MerlinEM pixelated detector (Quantum Detectors, Oxford, UK) with a convergence angle of $\sim 6 \text{ mrad}$. QSTEM software was used to perform 4D-STEM simulations of Ru-fcc and Ru-hcp nanoparticles with instrumental parameters matching the experimental ones. [46] Results were obtained after ten iterations of each simulation as a 10×10 grid of diffraction patterns. The patterns were then integrated to obtain an average diffraction pattern for each structure. Experimental 4D-STEM data was preprocessed with a natural logarithm to enhance lower-intensity features and then analyzed with the k-means clustering from the open-source scikit-learn library [47] to isolate individual nanoparticles and obtain their average diffraction patterns. X-ray photoelectron spectroscopy (XPS) measurements were performed with the Versa probe 3 AD (Phi, Chanhassen, MN, US) using a monochromatic Al K α X-ray source at an operating voltage of 15 kV and an emission current of 3.3 mA. Powder samples were placed on double-sided Scotch tape. Spectra were acquired on a $1 \times 1 \text{ mm}^2$ analysis spot size. During the measurements, the charge neutralizer was on. High-resolution (HR) spectra were measured at a pass energy of 27 eV and the binding energy (BE) step of 0.1 eV. Survey spectra were measured at a pass energy of 224 eV and the BE step of 0.8 eV. Every spectrum was acquired with at least 20 sweeps to improve the signal-to-noise ratio. The BE scale of XPS spectra was corrected using the C 1s peak at BE of 284.4 eV, corresponding to the partially graphitized carbon support (part) of the samples. Data processing (including peak fitting) was performed with the MultiPak 9.0 software. The Shirley background subtraction was used for all measurements. Three main doublet peaks were identified in the Ru 3d region for both Ru/C and Ru/TiON-C samples, corresponding to the Ru⁰, RuO₂, and RuO_x. The spin-orbit splitting value was kept constant at 4.17 eV for all the bands between Ru 3d_{5/2} and Ru 3d_{3/2}. The peak shape was chosen to be asymmetric for all species. The full width at half maximum (FWHM) was fixed for both samples at 0.7 for Ru⁰, 1.1 for RuO₂, and 1.4 for RuO_x.

2.3. Electrochemical characterization and HER investigations

For all catalysts (Ru/TiON-C, Pt/C, Ru/C, RuO₂, Ru/GO, Ru/TiON, and Ni/C), catalyst inks were prepared by mixing the catalyst powder with ultrapure water (18.2 M Ω cm) in a 1 mg/ml ratio. Mixtures were subjected to an ice-cooled ultrasonic bath for 30 min to obtain finely dispersed catalyst ink. Working electrodes were produced by pipetting 20 μ L of catalyst ink directly from the ultrasonic bath onto freshly polished glassy carbon rotating disk electrodes (Pine, 5 mm in diameter). After drying under clean ambient conditions, the catalyst films were covered with 5 μ L of Nafion (Sigma, 5 % solution in a mixture of lower aliphatic alcohols and water) diluted in isopropanol (1/50) to ensure good adhesion. The resulting loadings were 6.1, 10.2, and 20.4 μ g cm⁻² for Ru/TiON-C, Ru/C, and Pt/C, respectively, with respect to the metal (Ru or Pt).

Electrochemical characterization and HER investigations were performed in argon-saturated 1 M KOH electrolyte (Merck) in a classical thin-film rotating disk electrode setup (TF-RDE) unless stated otherwise. To avoid contamination by the glass corrosion, all electrochemical experiments in alkaline media were conducted in a Teflon cell, with a hydrogen reference electrode (Hydroflex from Gaskatel) and a glassy carbon rod as reference and counter electrodes, respectively. To ensure a reproducible baseline response before measuring activity, all catalyst

films were subjected to rapid voltammetric activation (300 mV/s, 50 cycles, 0.05 – 1 V_{RHE}) in the Ar-saturated 1 M KOH electrolyte. HER activities were measured by recording the polarization curves at a scan rate of 10 mV/s in the potential region from 0.1 to –0.2 V_{RHE} with iR compensation. Electrochemical impedance spectroscopy (EIS) was performed at HER overvoltage of 20 mV in the frequency range between 50 mHz and 100 kHz with an amplitude of 10 mV. The stability of Ru/TiON-C was measured by potential cycling (10,000 cycles, 100 mV/s) in the TF-RDE setup in a potential window between 0.2 and –0.1 V_{RHE}. The purpose of such a potential region is to avoid excessive bubble formation and provide time for the release of hydrogen bubbles formed during HER. The stability of Ru/TiON-C was also tested in a galvanostatic regime by applying a constant current density of 10 mA/cm² for 12 h. Furthermore, the durability of Ru/TiON-C was probed by a potential hold in a gas diffusion electrode (GDE) setup at an overvoltage of 30 mV. The GDE used for testing is a commercially available setup that has also been used in literature [48,49]. For GDE, the catalyst ink was prepared as a solution of a 1:1 volume-to-volume ratio of isopropyl alcohol and MilliQ water (resistivity 18.2 M Ω). The catalyst concentration was 1 mg/mL, and it was subjected to ultrasonication for 15 min to obtain a finely dispersed ink. Working electrodes were then prepared by spraying the catalyst ink onto the gas diffusion layer with a microporous layer (Sigracet 39BB, Fuel Cell Store) with an airbrush (Iwata). The catalyst loading that was obtained was 0.1 mg/cm². Chronoamperometry measurements were performed by holding the potential at –0.03 V_{RHE} for 4 h. The resistivity was not compensated due to the resistance being prone to change during the long-term experiment. Identical location STEM (IL-STEM) was performed to additionally study possible structural changes of Ru/TiON-C during HER operation. For this purpose, the modified floating electrode (MFE) setup was used [50]. The gold TEM grid was coated with 5 μ L of the catalyst ink, and the excess liquid was removed to ensure the formation of a very thin catalyst layer to enable easier IL-STEM imaging. Several locations of the pristine catalyst were imaged, and then the grid was mounted in MFE for a potentiostatic durability test performed at –0.05 V_{RHE} over 4 h in the same 1 M KOH electrolyte. The identical locations of the catalyst were imaged after the test to observe possible changes in the Ru/TiON-C nanostructure. Both GDE and MFE experiments are conducted in glass-free equipment made from Teflon. For comparison, HER activities of Pt/C, Ru/C, and Ru/TiON-C samples were also screened in an acidic electrolyte (0.1 M HClO₄). The method of underpotential deposition of Cu was used to determine the electrochemical surface area (ESA) of Ru/TiON-C and Ru/C samples [51]. These measurements were performed in 0.1 M H₂SO₄ in the absence and presence of 2 mM CuSO₄. The ESA was calculated by integrating the charge associated with Cu stripping after subtracting the baseline curve recorded in Cu-free electrolyte under the same conditions. The obtained charge was then converted to Ru surface area using a value of 420 μ C/cm², corresponding to a full monolayer of Cu on Ru. The ESA was calculated by normalization of the Ru surface area to Ru loading. In the case of Pt/C, ESA was determined by CO stripping voltammetry in 1 M KOH electrolyte [42]. For that purpose, CO was briefly introduced to the electrolyte while the electrode was held at 0.05 V_{RHE} to ensure CO adsorption, followed by Ar purging for 15 min to ensure CO removal from the electrolyte. The CO stripping voltammetry was recorded at a scan rate of 20 mV/s, followed by another CV to verify that the signal came only from adsorbed CO and to provide a baseline for ESA determination. After baseline correction, charge originating from CO stripping was calculated and compared with the value of 420 μ C/cm² corresponding to a full monolayer of CO on Pt. Finally, the determined Pt surface area was normalized by Pt loading to obtain ESA.

2.4. DFT calculations

DFT calculations were performed with Quantum ESPRESSO [52,53] using the Perdew–Burke–Ernzerhof (PBE) exchange–correlation

functional [54]. A plane-wave basis set with a cutoff of 50 Ry for the wave functions and 575 Ry for the charge density was used. Core electrons were described implicitly with projector-augmented-wave (PAW) potentials [55] from pslibrary [56,57]. For isolated nanoparticles and large supercell calculations, the Brillouin-zone integrations were performed with the gamma k-point and a Methfessel–Paxton smearing [58] of 0.02 Ry. Isolated Ru nanoparticles were calculated in a 25 Å large cubic box using the Makov–Payne correction [59]. This box size ensures that the distance between the nanoparticle's periodic replicas is at least 10 Å. Spin-polarized calculations were utilized for nanoparticles consisting of less than 30 Ru atoms. For larger nanoparticles, the effect of magnetization on energy was insignificant (less than 1 meV/atom). Two different supports were considered: carbon (C) and titanium oxynitride (TiON). For the C support, a graphene layer was used, described by a hexagonal unit cell with the calculated lattice parameters of $a = b = 2.467$ Å [42]. TiON was modeled as a $\text{Ti}_{1.5}\text{ON}(111)$ slab with three layers of Ti ions (the slab's structure is described in ref [41]). The graphene layer was modeled with the (7×7) supercell and the TiON support with the (3×3) supercell; the two supercells are of similar size, with a mismatch in lattice parameter being 2.5 %. A D3 dispersion correction of Grimme et al. [60] was utilized to better describe the adhesion of supported nanoparticles, and for TiON, a self-consistently calculated [61] U parameter [62,63] of 4.0 eV was used for Ti ions [41].

Ru nanoparticles (NPs) with the hcp and fcc structure were modeled, labeled respectively hcp-Ru_{*n*} and fcc-Ru_{*n*}, where *n* is the number of

atoms in the nanoparticle. Supported nanoparticles are labeled as hcp-Ru_{*n*}^{*m*} and fcc-Ru_{*n*}^{*m*}, where *m* is the number of Ru atoms in the bottommost nanoparticle's layer that faces the support.

For isolated nanoparticles, cohesion energies were calculated as:

$$E_{\text{coh}} = \frac{1}{n} (E_{\text{NP}} - nE_{\text{atom}}), \quad (1)$$

where E_{NP} is the energy of the isolated Ru_{*n*} nanoparticle, and E_{atom} is the energy of the isolated Ru atom. The adhesion of Ru nanoparticles on the graphene and TiON supports was characterized by the adhesion energy:

$$E_{\text{adh}} = E_{\text{NP/support}} - E_{\text{NP}} - E_{\text{support}}, \quad (2)$$

where the subscripts NP/support, NP, and support represent the Ru nanoparticle/support system, isolated Ru nanoparticle, and bare support, respectively. Additionally, a planar integrated electron density difference was calculated along the surface normal direction (*z*) according to:

$$\Delta\rho(z) = \int_A \Delta\rho(x, y, z) dx dy, \quad (3)$$

where *A* is the area of the surface supercell, and $\Delta\rho(x, y, z) \equiv \Delta\rho(\mathbf{r})$ is the 3D electron charge density difference calculated as:

$$\Delta\rho(\mathbf{r}) = \rho_{\text{NP/support}}(\mathbf{r}) - \rho_{\text{NP}}(\mathbf{r}) - \rho_{\text{support}}(\mathbf{r}), \quad (4)$$

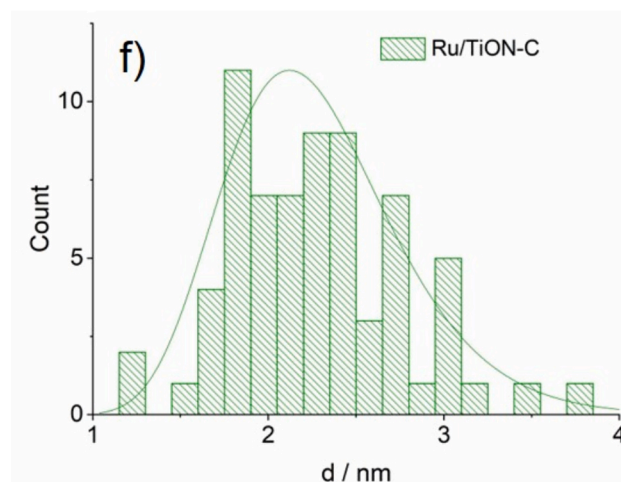
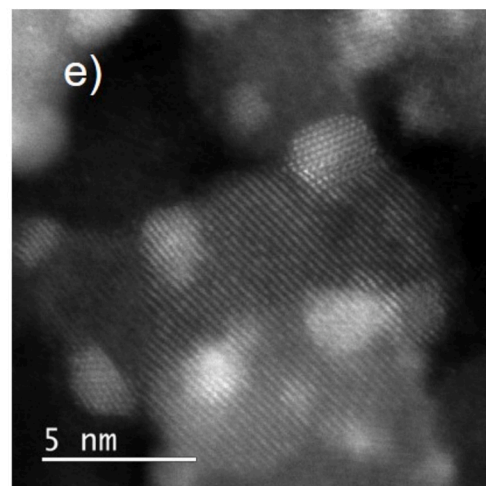
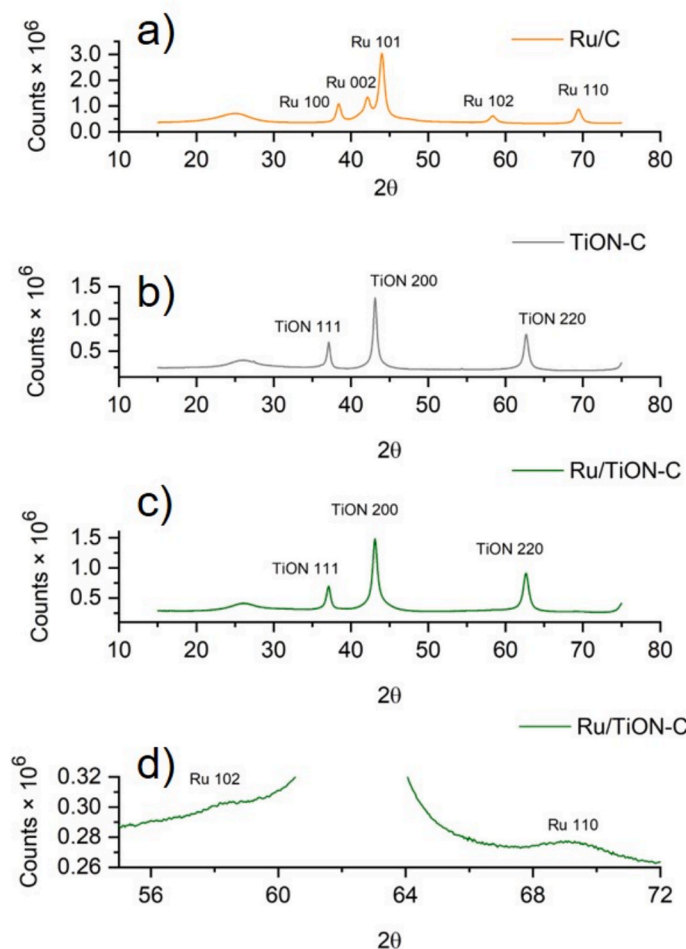


Fig. 1. Characterization of the Ru/TiON-C catalyst: The left panel shows XRD patterns; the right panel shows ADF-STEM imaging of Ru/TiON-C and particle size distribution.

with the standalone NP and support structures kept the same as in the NP/support system.

The average chemisorption energy of hydrogen was calculated as:

$$E_{\text{chem}} = \frac{1}{n} \left[E_{\text{nH/NP/support}} - E_{\text{NP/support}} - \frac{n}{2} E_{\text{H}_2} \right] \quad (5)$$

where $E_{\text{nH/NP/support}}$, $E_{\text{NP/support}}$, and E_{H_2} are the total energies of a supported nanoparticle with n adsorbed H atoms, a bare supported nanoparticle, and an isolated H_2 molecule, respectively.

3. Results and discussion

3.1. Characterization of Ru/TiON-C catalyst

The structural characterization of the Ru/TiON-C sample is given in Fig. 1. The XRD pattern of the Ru/TiON-C is presented together with the patterns of bare TiON-C composite and Ru/C analog (Fig. 1a-d). All characteristic peaks related to the usual hcp-Ru structure can be seen in the XRD pattern of Ru/C (Fig. 1a). STEM imaging of Ru/C revealed the presence of well-dispersed Ru nanoparticles (Fig. S1). Diffraction peaks corresponding to the cubic TiON support can be seen in patterns of both TiON-C and Ru/TiON-C (Fig. 1b and c); in the latter, they overlap with the Ru-hcp 100, 002, and 101 reflections, and mask them due to the much higher intensity. In the pattern of Ru/TiON-C, no pronounced Ru diffractions are visible. Close inspection reveals only very broad and low-intensity peaks at 2θ values of around 58.4° and 69.4° , which are not present in the pattern of the bare support (as highlighted in Fig. 1d). These peaks match 2θ values of 012 and 110 reflections of hcp-Ru, respectively. The low intensity and shape of these peaks indicate the presence of very small Ru particles with low loading in the Ru/TiON-C

sample. The presence of small-sized Ru nanoparticles is confirmed by the STEM imaging (Fig. 1e) and the corresponding particle size distribution showing an average diameter of around 2.1 nm (Fig. 1f). Elemental distribution in a representative region of the Ru/TiON-C sample was investigated using STEM-EDXS imaging. The results, shown in Fig. 2, confirm the presence of TiON, Ru, and carbon in the catalyst. The homogeneous distribution of Ti, N, O, and C indicates a uniform composition of the TiON-C support. Importantly, Ru nanoparticles are observed to preferentially anchor to the TiON phase rather than to the carbon component, suggesting a stronger interaction between Ru species and TiON than with the graphene template. This can be a hint towards MSI between TiON and Ru, which will be studied in more detail later on. A similar characterization can be found in our previous work in the case of the Pt/C used for benchmarking the HER performance [42]. In brief, commercial Pt/C (20 wt%, Premetek) contains Pt nanoparticles with an average diameter between 1–3 nm, which is very close to the particle size in the Ru/TiON-C sample.

To gain deeper insight into the interaction between TiON and Ru, X-ray photoelectron spectroscopy (XPS) was performed, and the collected data were compared with Ru/C, where significantly weaker interactions between carbon and Ru are expected. Survey spectra for Ru/C and Ru/TiON-C are presented in Fig. S2, while detailed deconvoluted analyses of C 1s and Ru 3d spectra are shown in Fig. 3. By fitting the spectra using the parameters described in the experimental section, three Ru species (Ru^0 , RuO_2 , and RuO_x) were identified in both Ru/C (Fig. 3a) and Ru/TiON-C (Fig. 3b), as summarized in Table S1.

The peak positions for Ru^0 , RuO_2 , and RuO_x in Ru/C were determined to be 280.15 eV, 280.95 eV, and 281.90 eV, respectively, while for Ru/TiON-C, the corresponding peaks were observed at 279.90 eV, 280.35 eV, and 281.35 eV. When the normalized Ru 3d spectra are

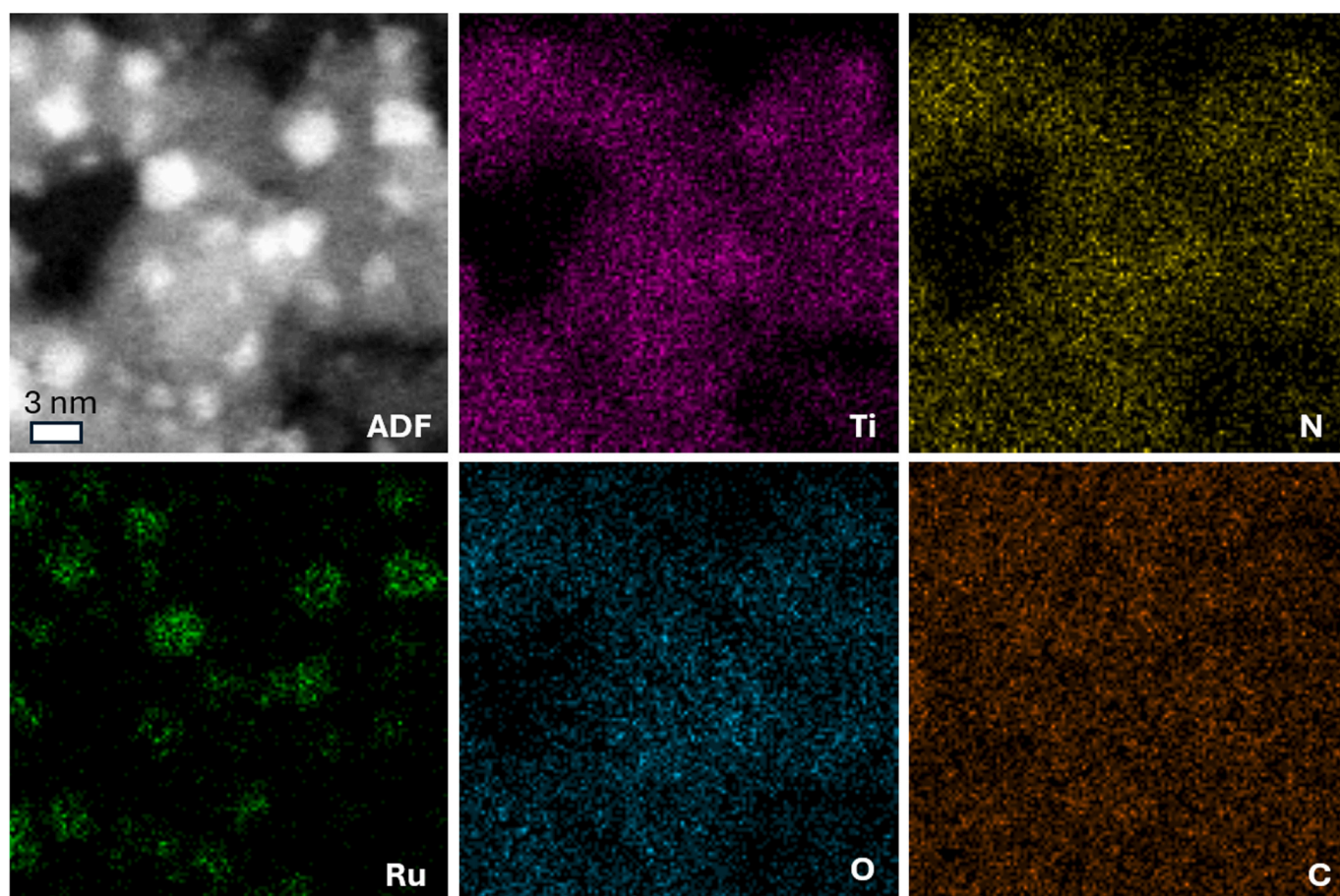


Fig. 2. ADF image and EDXS maps of the Ru/TiON-C sample illustrating the elemental distribution within the composite catalyst.

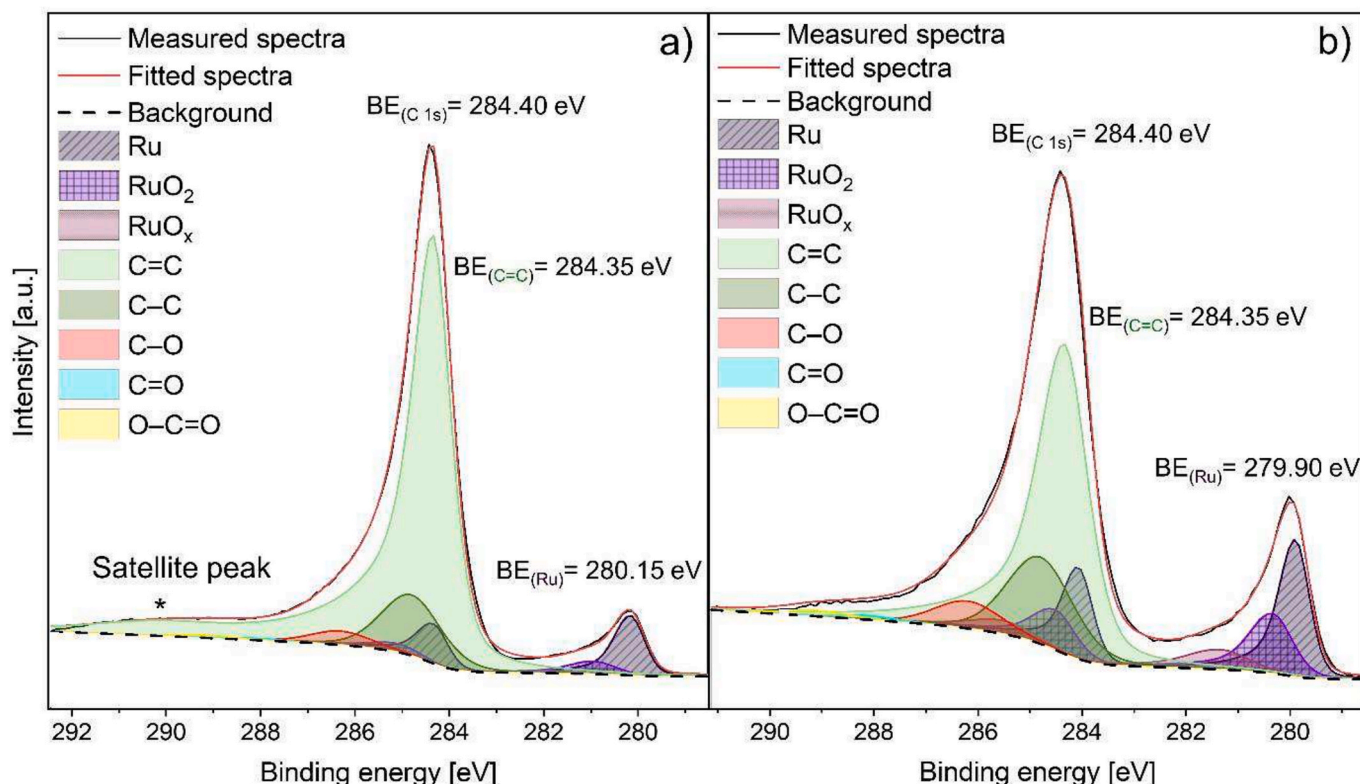


Fig. 3. Deconvoluted C 1s and Ru 3d spectra for samples (a) Ru/C and (b) Ru/TiON-C.

compared in Fig. 3 and Table S1, a distinct shift in the Ru^0 $3d_{5/2}$ peak position is evident. Specifically, the Ru^0 $3d_{5/2}$ peak for Ru/TiON-C (279.90 eV) appears at a lower binding energy (BE) compared to Ru/C (280.15 eV), with the Ru-oxide species exhibiting even more pronounced shifts. This observed 0.25 eV shift in BE for Ru^0 suggests a modified electronic interaction between Ru nanoparticles and their respective supports, with the stronger interaction in Ru/TiON-C likely arising from MSI. The consistent BE shift across all Ru species indicates a redistribution of electron density in Ru due to its interaction with the underlying TiON. Such electronic restructuring may effectively modulate the hydrogen adsorption/desorption characteristics of Ru active sites, thereby enhancing the kinetics of the HER [16,64].

Further investigation of the Ti 2p regions of bare TiON-C and Ru/TiON-C (Fig. S3, Table S2) revealed that their deconvoluted spectra are nearly identical, with the only notable difference being the presence of the $\text{Ru } 3p_{3/2}$ peak in the Ru/TiON-C sample. A comparison of the BE of Ti species shows a slight shift of all three species (Ti-N , Ti(O,N) , Ti^{4+}) by 0.05 eV toward lower BE in the Ru/TiON-C sample, which could be another indication of MSI. More subtle shift of Ti-species compared to the effect seen on Ru-species can be expected since these signals come from TiON interfaced with Ru nanoparticles, but also from TiON non-contacted with Ru. Since only a fraction of the TiON support is covered with Ru active sites, the overwhelming contribution from non-interfaced TiON (unaffected by MSI) dilutes the observable MSI effect. In contrast, most of the Ru particles are in contact with TiON, thus, the impact of MSI on Ru is more easily observed. Similar findings were reported in the work of Stühmeier et al., who studied the effect of a partial encapsulation of Ru particles with a thin overlayer of partially reduced TiO_x formed from TiO_2 support [65]. Authors commented that the interaction between TiO_x and Ru cannot be confirmed by analyzing Ti due to the dominant contribution from the non-interfaced TiO_2 . Additionally, analysis of the chemical composition (Table S3) indicates that TiON exhibits a similar Ti and N content in both TiON-C and Ru/TiON-C samples, while the TiON-C sample contains more oxygen and less

carbon.

3.2. Electrocatalytic HER investigations

The electrocatalytic HER performance of Ru/TiON-C in an alkaline electrolyte was compared with the Ru/C and Pt/C benchmark catalysts, as presented in Fig. 4. Collected polarization curves, given in Fig. 4a, reveal that the TiON-C support is inactive in the used potential range. The Ru/TiON-C sample is significantly more active than the Ru/C analog, which can be regarded as a clear indication of the support effect. More importantly, Ru/TiON-C is more active than the Pt/C benchmark with more than three times higher metal loading (6 wt% Ru vs. 20 wt% Pt). The overpotential needed to reach the current density of 10 mA cm^{-2} (η_{10}) is commonly used as a figure of merit for comparing the practical applicability of catalytic materials. The benchmark catalysts Ru/C and Pt/C exhibited η_{10} values of 102 mV and 45 mV, respectively, which are consistent with literature reports for similar systems [66,67]. However, comparison with literature data needs special attention as the metal loading can strongly influence the obtained η_{10} values. For example, Zhao et al. reported significantly lower η_{10} values: 40 mV for 20 wt% Ru/C and 26 mV for 40 wt% Pt/C [36]. These results were obtained using a much higher total catalyst loading of 0.398 mg cm^{-2} compared to 0.102 mg cm^{-2} in our study, while the loading of Pt and Ru in their reference catalysts was also higher. As a result, the higher density of Ru and Pt active sites in their measurements enhances the apparent catalytic HER performance, which will be inversely correlated with intrinsic or mass activity. In the case of Ru/TiON-C, η_{10} value of 42 mV was obtained, which is beyond both carbon-supported benchmarks. Mass activity (MA) of these catalysts can illustrate their techno-economic viability and is the most relevant parameter for practical applications. A comparison of the MAs of the Ru/TiON-C, Ru/C, and Pt/C samples, Fig. 4b, showcases the superior performance of Ru/TiON-C. At the overpotential of 100 mV, Ru/TiON-C delivers MA of $6505 \text{ A g}_{\text{Ru}}^{-1}$, which is around 6.8 and 4.5 times higher than for Ru/C and Pt/C,

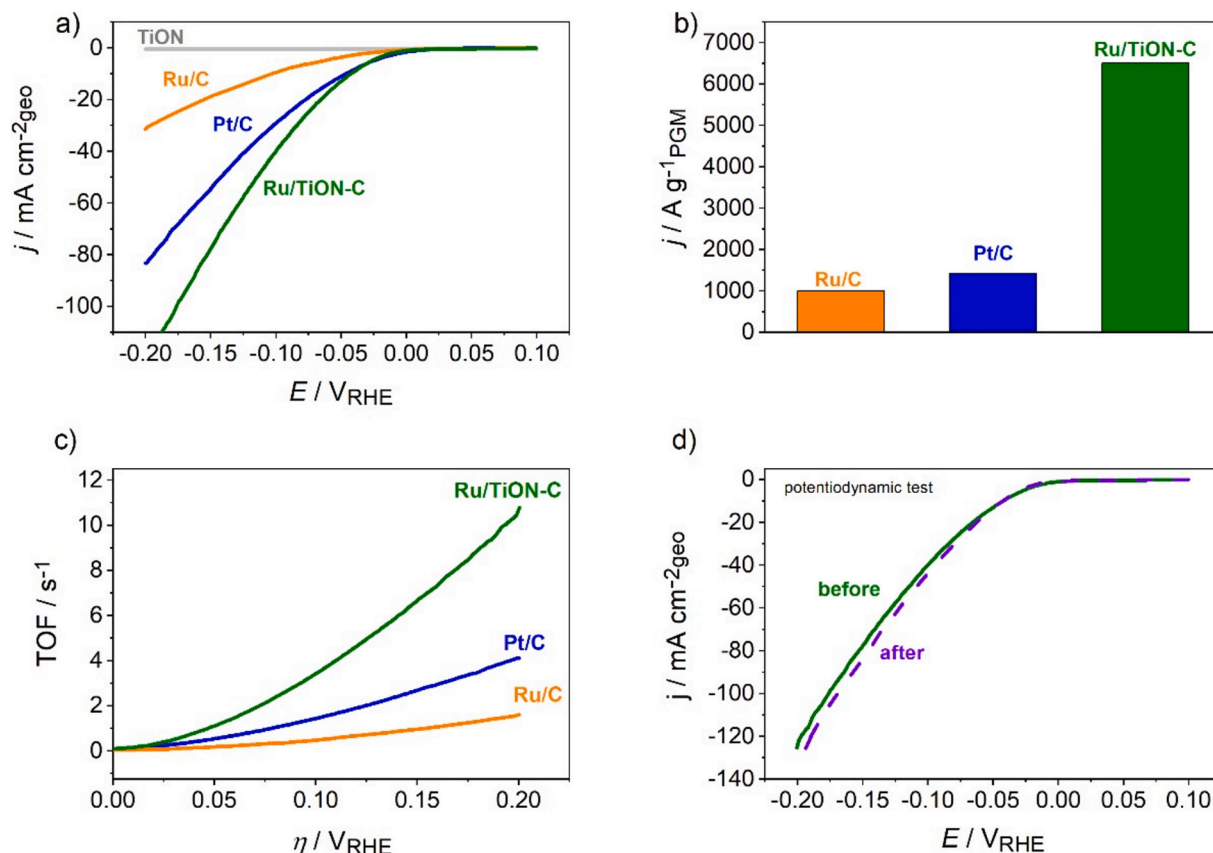


Fig. 4. Comparison of the HER activities of the Ru/TiON-C, Ru/C, and Pt/C catalysts: (a) HER polarization curves (Ar-saturated 1 M KOH, 10 mV/s); (b) mass activities at an overpotential of 100 mV; (c) turnover frequencies; (d) comparison of HER activity of Ru/TiON-C before and after potentiodynamic stability test (10 000 scans, 100 mV/s, potential window between 0.2 and -0.1 V/RHE).

respectively.

More insights into the intrinsic HER activity can be obtained by evaluating the turnover frequencies (TOF) of the compared catalysts [68]. TOF values were calculated using the following equation:

$$\text{TOF} = \frac{i}{2Fn} \quad (6)$$

In Eq. (6), i stands for measured HER current, F is the Faraday constant (96,485 C/mol), factor 2 stands for two electrons exchanged to form a H₂ molecule, and n is the number of moles of the active metal sites. The number of moles (n) was calculated based on the metal loading in the catalyst (determined by ICP-OES) and the mass of catalyst deposited on the electrode. This methodology considers that the total catalyst loading is active in the reaction, meaning that the obtained TOFs are lower-bound values. Nevertheless, the similarity of investigated catalysts makes TOF a relevant comparison point, Fig. 4c, which reveals a dominant intrinsic activity of Ru/TiON-C compared to carbon-supported benchmarks. Additional assessment of the intrinsic activities can be achieved using electrochemical surface area to normalize measured HER polarization curves. In the case of Ru/C and Ru/TiON-C, ESA values of 50.1 and 92.8 m²/g were determined by the method of underpotential deposition of copper [51] (Fig. S4), while for Pt/C, ESA of 84.5 m²/g was obtained through CO stripping voltammetry (Fig. S5). Fig. S6 shows significantly higher ESA-normalized current for Ru/TiON-C compared to Pt/C and Ru/C.

Insights into HER kinetics on Ru/TiON-C and carbon-supported catalysts are provided in Fig. S7. Tafel analysis was performed in the low overpotential region ($\eta \leq 50$ mV) to ensure that only kinetic contributions were evaluated, revealing a Tafel slope of approximately 40 mV/dec for Ru/TiON-C, similar to that of Pt/C, which corresponds to the

Volmer–Heyrovsky pathway (Fig. S7a). In contrast, the slope of 60 mV/dec was fitted for Ru/C, indicating slower reaction kinetics and charge transfer on Ru sites contacted with carbon. Electrochemical impedance spectroscopy, Fig. S7b, shows a significantly lower charge transfer resistance for the Ru/TiON-C composite than for Pt/C and Ru/C, agreeing with activity and Tafel slope trends.

Comparison of the performance of Ru/TiON-C composite with industrially viable materials, such as Ni-based catalysts, is given in Fig. S8. It can be seen that Ru/TiON-C is significantly more active than a commercial Ni/C (20 wt% from Premetek), which needs 270 mV higher overpotential to deliver the current density of 10 mA cm⁻².

To clarify the role of the components of the support matrix, we compared the HER activity of Ru nanoparticles deposited on graphene oxide (Ru/GO) and titanium oxynitride (Ru/TiON) with that of the Ru/TiON-C composite. The performance of Ru/GO was lower than that of Ru/TiON-C and comparable to Ru/C, indicating that the type of carbon support does not significantly affect catalytic activity (Fig. S9a). Interestingly, Ru/TiON without the carbon template exhibited lower HER performance than Ru/GO and Ru/C. This can be attributed to the agglomeration of TiON particles in the absence of a carbon template, limiting the overall surface area and leading to poor Ru dispersion. XRD spectra of Ru/TiON (Fig. S9b) confirm this claim and indicate the presence of significantly larger Ru nanoparticles than in Ru/TiON-C (see Fig. 1c and d). In addition, the Ru/TiON sample without a carbon template may be challenged with obstructed electron pathways, which would be particularly pronounced with low Ru-loadings. These findings emphasize that while MSI between Ru and TiON contributes to enhanced HER activity, this effect is only realized when TiON is integrated within a conductive carbon framework. The Ru/TiON-C composite thus optimally combines electronic effects from MSI with

improved nanoparticle dispersion and conductivity.

To investigate if the MSI provided by TiON shows a similar effect on the performance of Pt in alkaline media, we screened the alkaline HER features of the Pt/TiON-C catalyst (Fig. S10). It can be seen that Pt/TiON-C shows only a slight activity enhancement compared to Pt/C (Fig. S10a), which can be ascribed to the improved hydrogen adsorption energetics (as shown for acid electrolyte in our recent work [42]) rather than reducing the water dissociation barrier. Ru/TiON-C is slightly more active than the Pt/TiON-C analog (Fig. S10a), and much better in terms of metal utilization (Fig. S10b). This comparison shows that the interaction between TiON and Ru is much more pronounced than in the case of Pt, leading to a substantial enhancement in HER activity.

A comparison of the main HER activity descriptors for Ru/TiON-C in alkaline media with the literature data on the high-performing Ru-based catalysts is given in Table 1. The first highlight of our Ru/TiON-C composite is the significantly lower mass of Ru as the active compound with respect to the loadings used across the literature (note that in some cases, Ru loadings are not even reported). Our catalyst provides a comparable η_{10} value with literature data, although there are some impressively low reported overvoltages, for instance, 15 mV, 17 mV, and 5 mV for Cu-Ru alloy [16], Ru@C₂N catalysts [69], and Ru single atoms and nanoclusters [70], respectively. However, as discussed earlier, this parameter may not always reflect the intrinsic activity, as it can be substantially affected by the loading of the catalyst [6,16]. This effect is showcased for Ru/TiON-C in Fig. S11, where one can see that increased loading of the catalyst resulted in the lowering of the overpotential, but at the same time, MA notably decays. Therefore, we focus more on keeping the loading of our catalyst low and comparing the intrinsic HER activity and techno-economic viability through the TOF and MA values in Table 1. In that regard, the Ru/TiON-C composite significantly surpasses most current literature reports on various Ru-based materials listed in Table 1, and even with Ru-single atom catalysts, known for maximizing metal utilization [70,71].

Probing the durability of materials for gas-evolving reactions is always challenged by the formation of microbubbles attached to the active sites [77,78]. To alleviate this issue as much as possible, the stability of the Ru/TiON-C catalyst during HER was examined in different conditions, namely potentiostatic, galvanostatic and potentiodynamic, and different setups, namely TF-RDE, GDE, and MFE. Extensive potential cycling (10,000 cycles, 100 mV/s, potential region between 0.2 and $-0.1 V_{RHE}$) was performed in the TF-RDE setup, Fig. 4d. To minimize the impact of microbubbles formed during the test, we periodically used (at every 250 HER scans) a few rapid potential cycles between 0.05 and $1 V_{RHE}$ to promote oxidation and release of potentially trapped hydrogen bubbles in the catalyst layer. Results obtained at the end of this test indicate stable HER running with no activity decay. Slight enhancement observed at the end of the degradation test can be ascribed to some non-intrinsic factor, such as the change of the local resistance and enhanced removal of the microbubbles. We made several attempts to measure the stability of our catalyst in potentiostatic/galvanostatic regimes in TF-

RDE, and all tests revealed rapid activity decay (within minutes) as a consequence of visible surface blockage by the formed hydrogen bubbles even at high rotation rates. To reduce the thickness of the catalyst film and thus the trapping of hydrogen bubbles, we diluted the catalyst ink five times and measured the durability in the galvanostatic regime (Fig. S12a). After the initial stabilization period, the E-t curve remained fairly stable for the test duration of 12 h. Even in the case of a much thinner catalyst film and high rotation speed, accumulation and detachment of bubbles caused the periodic spikes in the chronopotentiometric curve. GDE arrangement is closer to the realistic membrane electrode assembly as it improves the mass transport of gaseous reactants or products, as opposed to RDE [48]. For this reason, we exposed Ru/TiON-C to an HER overvoltage of 30 mV in a GDE assembly [48,49]. Ru/TiON-C exhibited quite stable HER running during the potential hold with negligible current decay (see Fig. S12b), however, it can be seen how the microbubble formation affects the durability assessment even in GDE (see the sharp current drops in Fig. S12b after approximately 1.5 and 3 h). To confirm the structural stability of Ru/TiON-C during HER operation, catalyst ink was deposited on the TEM grid and exposed to a potentiostatic hold at $-0.05 V_{RHE}$ in the MFE setup. An identical location STEM (IL-STEM) study was performed by collecting STEM images on the same locations on the catalyst surface before and after the degradation test, Fig. 5. Degradation of nanocatalysts during HER is commonly caused by the weak interaction between carbon support and nanoparticles, resulting in particle migration, detachment, and/or agglomeration [35,42,79]. IL-STEM imaging reveals that the Ru/TiON-C composite remained stable during the potentiostatic test and that neither of the mentioned degradation mechanisms took place to a notable extent. This finding is particularly valid for Ru particles attached to TiON flakes, where no discernible degradation occurred (a few examples of stable locations are labeled by matching color circles in Fig. 5). As shown below with DFT calculations, TiON anchors the Ru particles considerably stronger than carbon, which inhibits their migration during HER in a similar manner as for the Pt/TiON composite [42]. Only a few very subtle changes in the catalyst nanostructure can be seen, which are marked by white and purple arrows in Fig. 5. In both cases, based on the STEM bright field (BF) and angular dark-field (ADF) images, it can be speculated that these particles migrated over carbon (and not TiON). A few similar examples of particle migration over carbon can be observed in IL-STEM images with lower magnification, Fig. S13.

Furthermore, we investigated the activity of Ru/TiON-C for HER in acid media (Fig. S14). Ru/TiON-C is significantly more active than Ru/C, indicating a favorable adjustment of the ΔG_{H^*} parameter of Ru-sites via the support effect. Expectedly, Ru/TiON-C did not surpass the activity of Pt/C, suggesting that its ΔG_{H^*} parameter is placed between Ru/C and Pt/C. Since Ru-based catalysts are widely explored for OER as alternatives to extremely scarce Ir, and the utilization of advanced supports in OER is very important [30], we compared the OER activity of Ru/TiON-C with the Ru/C and unsupported RuO₂ benchmark (Fig. S15).

Table 1
Comparison of the HER performance of Ru/TiON-C with literature data.

Parameter Catalyst	Loading ($\mu\text{g}_{\text{Ru}} \text{ cm}^{-2}$)	η_{10} (mV)	Tafel slope (mV dec ⁻¹)	TOF (#H ₂ site ⁻¹ s ⁻¹)	MA (A g ⁻¹)
Ru/C-TiO ₂ [72]	200	44	73.7	0.0223 (/ mV)	/
Ru/C ₃ N ₄ /C [27]	40.8	79	/	4.2 (@ 100 mV)	/
Ru/g-C ₃ N ₄ [73]	/	34	27	0.51 (@ 50 mV)	322 (@50 mV)
Ru-Cr ₂ O ₃ /NG [74]	150	47	39	6.4 (@ 100 mV)	/
Ru@Co/N-CNT [75]	/	48	33	/	/
Cu-Ru alloy [16]	306	15	30	1.139 (@100 mV)	199.59 (@50 mV)
Porous Pd@Ru [76]	102 (Pd + Ru)	30	30	/	722.9 (@60 mV)
Ru@C ₂ N [69]	285	17	38	1.66 (@50 mV)	/
Ru single atoms and nanoclusters [70]	20	5	55	5.34 (@100 mV)	4220 (@ 50 mV)
Atomically dispersed Ni-Ru-P [71]	/	57	75	3 (@95 mV)	1134 (@57 mV)
Ru/TiON-C (this work)	6.4	42	40	3.5 (@100 mV)	2167 (@ 50 mV)

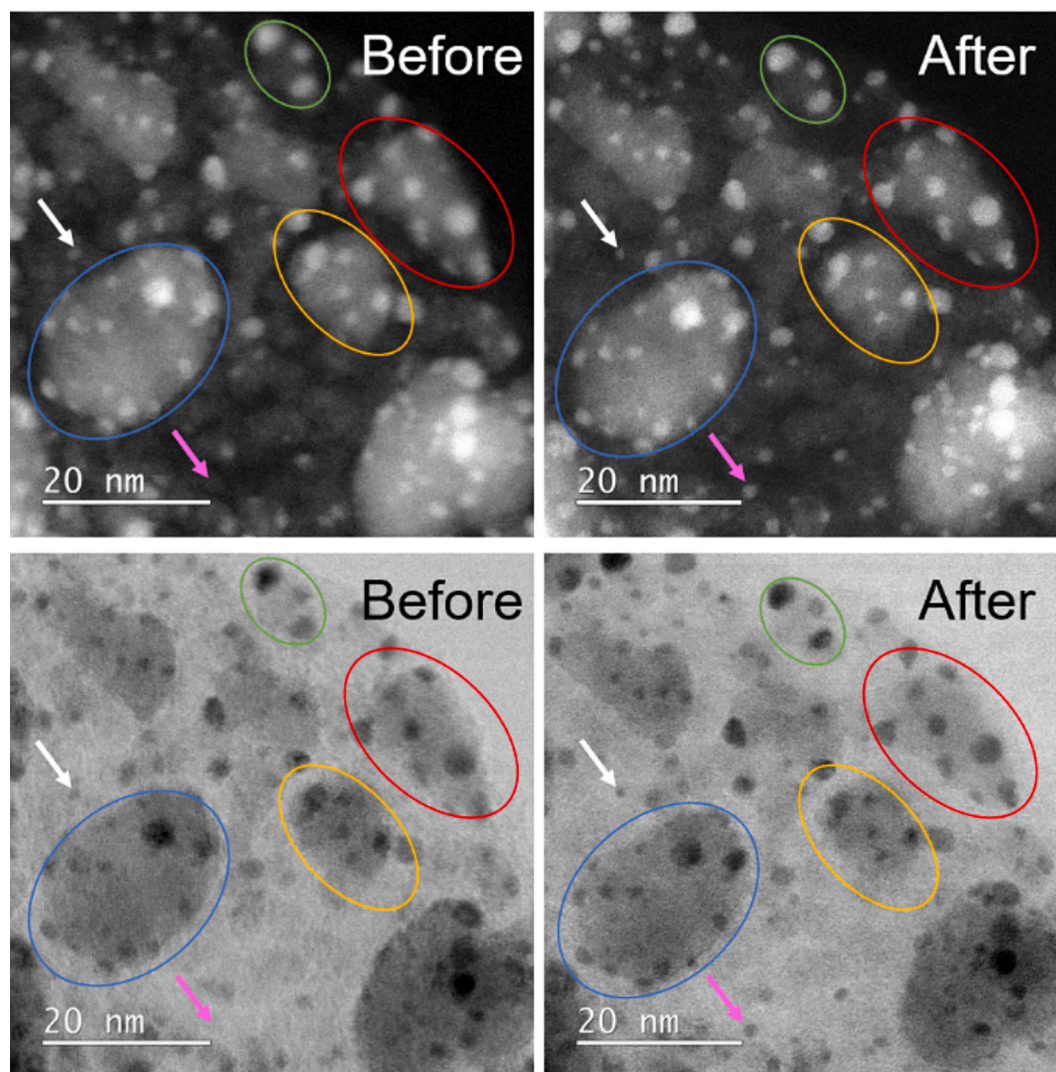


Fig. 5. ADF and BF IL-STEM imaging of the Ru/TiON-C sample exposed to potentiostatic degradation test in MFE setup (4 h at $-0.05 V_{RHE}$, 1 M KOH).

These preliminary results show that both supported Ru-catalysts surpass RuO_2 (Fig. S15a), which can be explained by the presence of metallic Ru species in Ru/C and Ru/TiON-C, known for their high OER activity, but also extremely rapid dissolution [80]. In terms of mass-normalized activity, Ru/C and Ru/TiON-C show comparable performance, which is significantly higher than that of RuO_2 (Fig. S15b), showcasing the benefits of using supported nanocatalysts. However, carbon support (in Ru/C sample) is problematic in OER catalysis due to carbon corrosion and consequent catalyst deactivation, whereas TiON support offers stability under OER operation, which can be further combined with MSI to improve the performance of active sites [30,41]. Therefore, these results show that the Ru-TiON platform can be taken as a promising baseline for additional material engineering (i.e., deposition of RuO_2 nanoparticles instead of metallic Ru, increased loading, further support adjustments, etc.) to build advanced OER catalysts.

To unravel the origin of the high HER activity of Ru/TiON-C composite, we compared HER activities in acid and alkaline media for Pt/C, Ru/TiON-C, and Ru/C catalysts, Fig. S16. For highly active Pt/C, HER in alkaline media is strongly hampered compared to acid due to the high energy barrier for water dissociation, as illustrated in Fig. S16a. In contrast, although the Ru/C electrode is significantly less active than Pt/C, its HER activities in acid and alkaline electrolytes coincide, Fig. S16b. This can be explained by unfavorable hydrogen adsorption strength on Ru as the main factor limiting HER activity, combined with facile water

activation. Similar behavior is observed for Ru/TiON-C but with much higher HER activities in both acid and alkaline electrolytes, Fig. S16c. Thus, it can be proposed that MSI between Ru and TiON affects both key descriptors for HER activity in a way that hydrogen adsorption energy is favorably adjusted (as confirmed by HER tests in acid media, Fig. S14), while water activation is facilitated so that it does not induce any additional kinetic penalty. It was reported earlier that thermodynamically unfavored fcc-Ru structures, enabled by the strong interaction with the support material have excellent water dissociation properties and thus high HER activities in alkaline media [27]. The local crystal structure of selected regions of the catalyst and, therefore, the possible presence of different Ru crystal structures in Ru/TiON-C was investigated with 4D-STEM (Fig. 6). Experimental 4D-STEM data was obtained for two regions of interest that included Ru nanostructures on TiON-C (Fig. 6b). In both cases, Ru nanostructures were imaged in a zone axis to obtain adequate diffraction contrast. The k-means clustering algorithm was used to segment the nanoparticle diffraction patterns from the rest of the data to isolate them from the TiON support. The nanoparticle diffraction patterns were integrated to yield an average nanoparticle pattern, and distances and angles between series of Bragg disks were measured to deduce the imaging zone axis (Fig. 6d). Then, the average nanoparticle diffraction patterns were compared to the simulated diffraction data of different Ru structures in their respective zone axes (Fig. 6e). In one instance, the nanoparticle average diffraction pattern

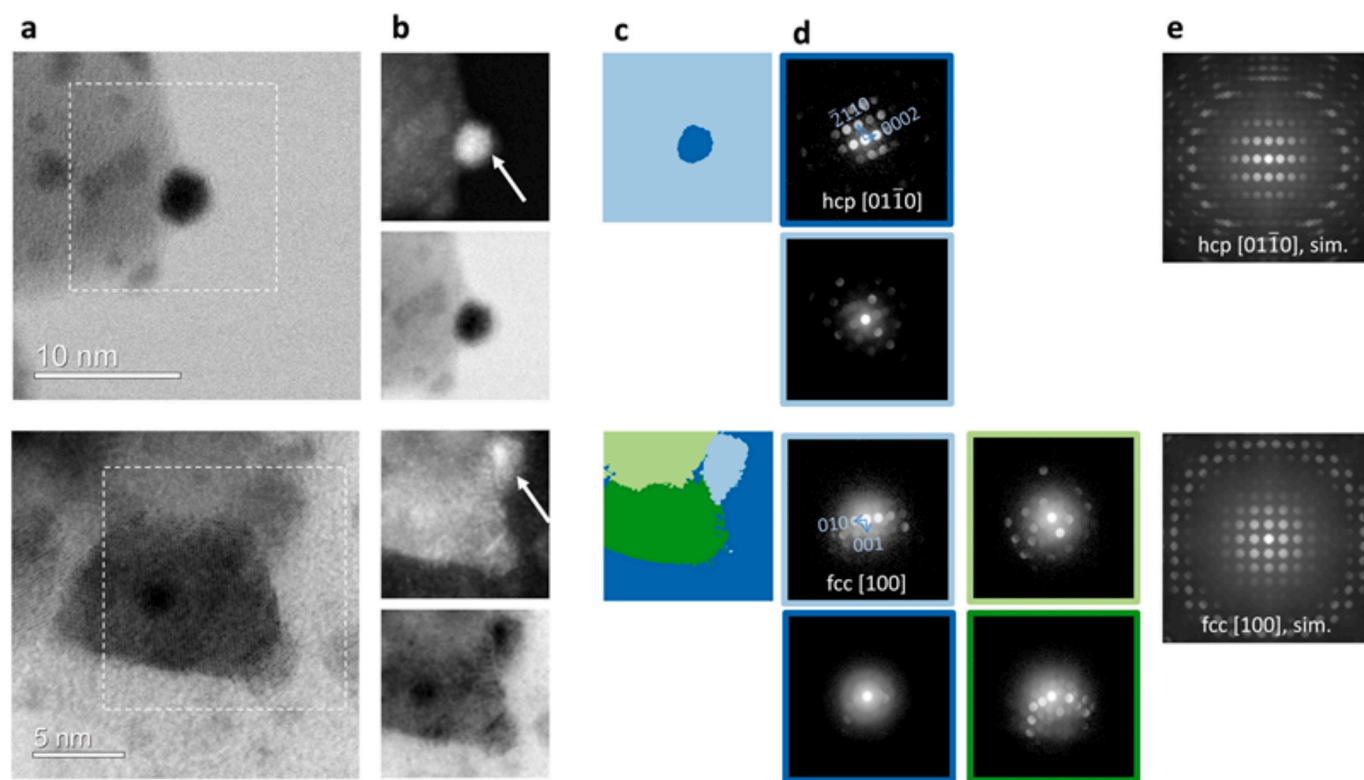


Fig. 6. 4D-STEM of an hcp-Ru (upper) and a proposed fcc-Ru (lower) nanoparticle. (a) BF-STEM images with white dashed rectangles denoting the 4D-STEM imaging area. (b) Virtual dark-field (upper) and bright-field (lower) reconstructions from the 4D-STEM data. White arrows denote the studied nanoparticles. (c, d) Clustering results with color-coded labels (c) and the cluster average diffraction patterns with a border matching their label, showing distinct crystal structures present within each region of interest (d). Arrows show a 90° angle between Bragg disks. (e) Simulated diffraction patterns of Ru structures in zone axes most closely matching experimental results.

was consistent with an hcp-Ru structure, and in another, the data suggest the presence of a small fcc-Ru nanoparticle, characterized by Bragg disks assuming positions of an fcc structure in a [100] zone axis. Therefore, the suspected presence of fcc-Ru nanostructures could be responsible for the boosted HER performance of the Ru/TiON-C in alkaline media. Since the Ru/TiON-C catalyst is more active for HER than Ru/C benchmark in acid media (where water dissociation does not take place, thus eliminating the effect of fcc-Ru), it can be proposed that MSI also affects hydrogen adsorption on predominant hcp-Ru sites. MSI between Ru and TiON and its versatile impact on HER performance is further scrutinized below using DFT calculations.

3.3. DFT calculations

Before examining the MSI effect with DFT calculations, let us validate the preceding experimental analysis of the feasibility of fcc-structured Ru nanoparticles. Ru is an hcp metal, and according to the current calculations, the hcp-Ru bulk is by 0.11 eV/atom more stable than the fcc-Ru bulk. In contrast, for small nanoparticles of up to about 200 atoms, the stability difference between hcp and fcc nanoparticles is insignificant, as revealed by Fig. 7, which shows the cohesive energy as a function of the number of atoms in the nanoparticle. The cohesive energy decreases with increasing nanoparticle size, asymptotically approaching the bulk values. However, even for the largest calculated nanoparticle (~200 atoms), the hcp and fcc fitting curves are almost superimposed, indicating similar stability of the hcp and fcc nanoparticles. This result implies that both hcp- and fcc-type structures are thermodynamically feasible for small nanoparticles (with a diameter of up to 2 nm corresponding to the largest calculated nanoparticles).

To examine MSI using DFT, we calculated the adhesion of Ru nanoparticles on the TiON and graphene supports. Fig. 8 shows the

planar integrated electron density differences along the surface normal direction ($\Delta\rho(z)$), 3D electron density differences ($\Delta\rho(r)$), and adhesion energies (E_{adh}) of the hcp-Ru₅₄^{6} nanoparticle on both supports, where the superscript {6} represents the number of Ru atoms in the bottom-most nanoparticle's layer that adheres to the support. The nanoparticle adheres four times stronger to the TiON support (−16.3 eV/nanoparticle, corresponding to −2.7 eV/Ru atom) than to graphene (−4.1 eV/nanoparticle, corresponding to −0.7 eV/Ru atom). Also, the $\Delta\rho(z)$ and $\Delta\rho(r)$ plots witness a substantially stronger redistribution of electron charge for TiON. We can see an electron surplus in the bonding region between the support and the nanoparticle on both supports. However, the electron accumulation is much stronger for TiON, where the electron charge displaces from the upper layer of Ti ions and the bottom layer of Ru atoms toward the Ru/TiON interface region, forming a pronounced electron accumulation. Such pronounced charge redistribution indicates strong MSI between the TiON support and Ru nanoparticles, which can enhance the durability of the catalyst and the HER activity [42,58].

Further analysis of the nanoparticle adhesion and stability is provided in Fig. 9, which shows the results for two hcp and two fcc nanoparticles supported on graphene and TiON. These nanoparticles were chosen in pairs, and within the pair, the hcp and fcc nanoparticles are mutually comparable because they have the same two bottom layers, where the bottommost layer is the layer that adheres to the support. In particular, hcp-Ru₃₈^{7} vs fcc-Ru₃₈^{7} and hcp-Ru₅₄^{6} vs fcc-Ru₅₄^{6} pairs are considered (the adhesion positions of these nanoparticles are schematically shown in Fig. S16 in the Supporting information). TiON binds these nanoparticles about four times stronger than graphene, thus immobilizing and stabilizing them.

As for the hcp vs fcc adhesion preference, the hcp nanoparticles adhere to graphene by 0.3 eV more strongly than the fcc nanoparticles.

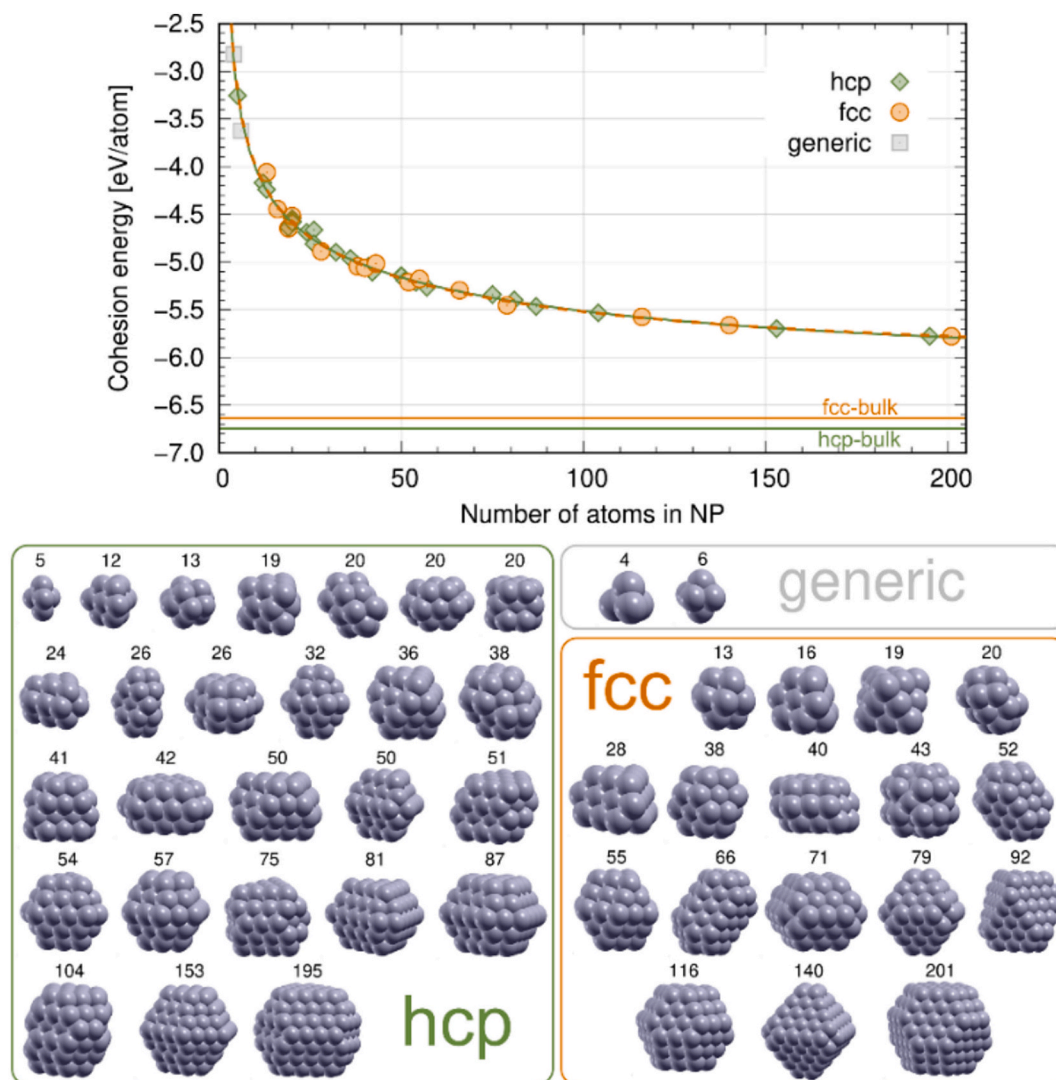


Fig. 7. Top: calculated cohesion energies as a function of the number of atoms in a nanoparticle for hcp and fcc Ru nanoparticles (tetrahedral Ru₄ and octahedral Ru₆ are consistent with the hcp and fcc structures and are therefore labeled as generic (gray squares)). Green is used for hcp and orange for fcc nanoparticles. The two curves represent the fits for hcp and fcc Ru nanoparticles. In contrast, the two solid lines represent the calculated cohesion energies for hcp and fcc Ru bulk. Bottom: snapshots of the considered nanoparticles. (For interpretation of the references to color in this figure legend, the reader is referred to the web version of this article.)

In contrast, on the TiON support, fcc-Ru₃₈⁽⁷⁾ binds by 0.7 eV stronger than hcp-Ru₃₈⁽⁷⁾, but vice-versa is true for the Ru_n⁽⁶⁾ nanoparticles because hcp-Ru₅₄⁽⁶⁾ adheres by 0.4 eV stronger than fcc-Ru₅₅⁽⁶⁾. These results may suggest that hcp nanoparticles adhere more strongly to graphene than fcc nanoparticles and that the adhesion preference on TiON depends on the nanoparticle's shape. However, the number of cases considered is far insufficient to reach any statistically valid conclusion. We can thus only infer from the current DFT results that fcc-structured Ru nanoparticles supported on TiON may exist. Combined with the STEM analysis (Fig. 6), this allows for a distorted Ru-fcc structure in the Ru/TiON-C composite.

To examine the effect of the support on hydrogen chemisorption energy, we performed two types of adsorption calculations. First, we investigated the chemisorption energy of a single H atom on various adsorption sites of the hcp-Ru₅₄⁽⁶⁾ nanoparticle supported on TiON and graphene. To this end, we tested 44 initial H adsorption structures for TiON and 41 for graphene, resulting in 27 optimized structures on each support, as some initial structures converged to the same optimized configuration. The corresponding H chemisorption energies are presented in Fig. S17, while snapshots of the optimized adsorption structures are shown in Figs. S18 and S19 in the Supporting Information.

Although noticeable differences in chemisorption energy exist between the two supports, the values range from -0.8 to -0.2 eV without a clear discernible trend (Fig. S17). Since these results provide limited insight into the role of support on H chemisorption energy, we also conducted calculations where the hcp-Ru₅₄⁽⁶⁾ nanoparticle was fully covered with H atoms. This setup better reflects conditions relevant to active hydrogen evolution, where nanoparticles are expected to be highly covered by chemisorbed H atoms. The optimized structures with 76 H atoms adsorbed on hcp-Ru₅₄⁽⁶⁾ nanoparticle supported on TiON and graphene are shown in Fig. 10. The corresponding average H chemisorption energies are -0.456 and -0.471 eV per H atom for hcp-Ru₅₄⁽⁶⁾ on TiON and graphene, respectively. These values suggest that the interaction between TiON and Ru marginally weakens the average H chemisorption energy by 150 meV compared to the graphene case. According to the volcano plot concept, Ru binds H too strongly [14,81], and the observed weakening of H binding should facilitate H₂ formation to some extent, potentially enhancing the activity of the Ru/TiON-C catalyst. This finding aligns with our previous study on the effect of TiON support on Pt nanoparticles [42], where the impact of the support on H chemisorption energy was analyzed in greater detail. This result is reasonable, as it is well known that supports that strongly bind metal

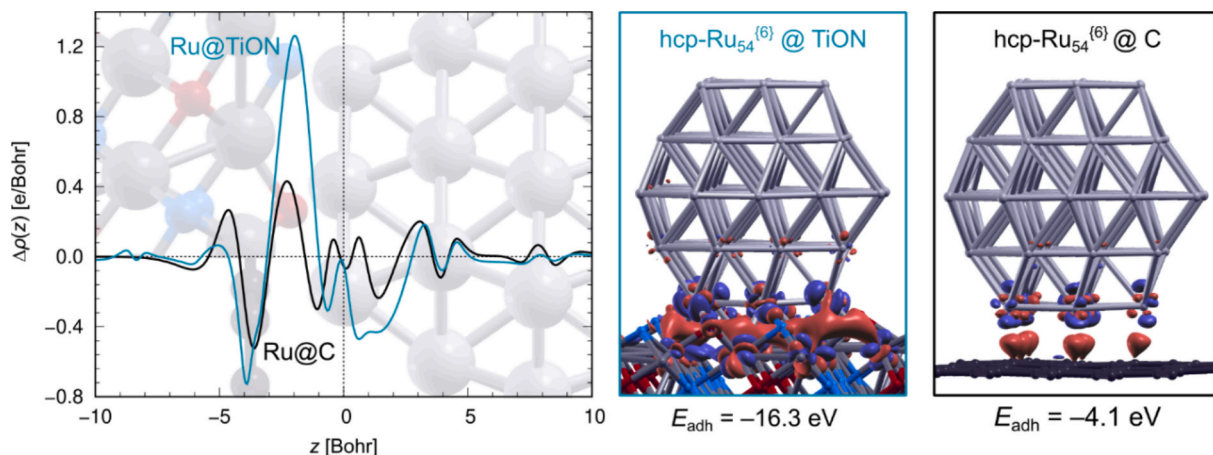


Fig. 8. Left: the planar integrated electron density difference for the hcp-Ru₅₄^{6} nanoparticle on the TiON and graphene supports, $\Delta\rho(z)$ calculated with eq (3). A nanoparticle/support structure is shown as a watermark behind the $\Delta\rho(z)$ curves to facilitate interpretation; $z = 0$ is set at the position of the bottommost Ru layer that adheres to the support. Right: the snapshots of the hcp-Ru₅₄^{6} nanoparticle supported on TiON and graphene along with the superimposed 3D electron density difference, $\Delta\rho(r)$ calculated with eq (4); isosurfaces of ± 0.01 e/Bohr³ are plotted with the red (blue) color representing electron excess (deficit). The respective adhesion energies are also reported. (For interpretation of the references to color in this figure legend, the reader is referred to the web version of this article.)

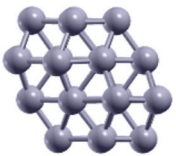
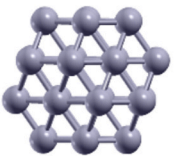
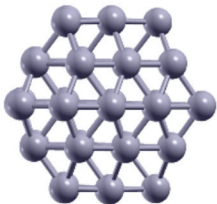
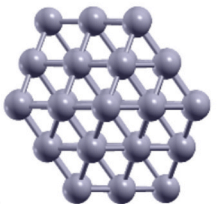
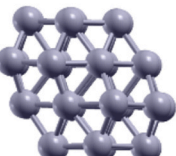
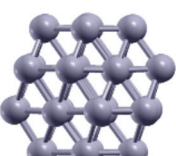
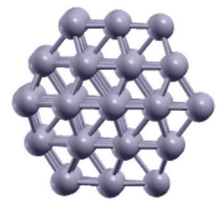
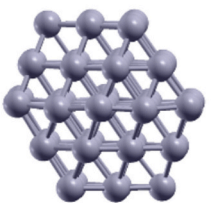
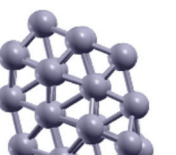
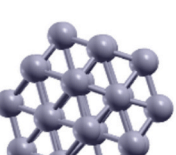
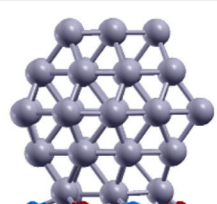
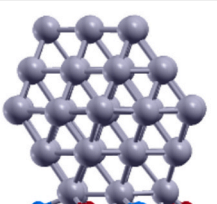
	hcp-Ru ₃₈ ^{7}	fcc-Ru ₃₈ ^{7}	hcp-Ru ₅₄ ^{6}	fcc-Ru ₅₅ ^{6}
isolated				
	$E_{\text{coh}} = -5.03$ eV/atom	-5.04 eV/atom	-5.21 eV/atom	-5.18 eV/atom
C				
	$E_{\text{adh}} = -4.3$ eV/NP	-4.0 eV/NP	-4.1 eV/NP	-3.8 eV/NP
TiON				
	$E_{\text{adh}} = -17.0$ eV/NP	-17.7 eV/NP	-16.3 eV/NP	-15.9 eV/NP

Fig. 9. Top row: snapshots and cohesion energies (E_{coh}) of standalone hcp-Ru₃₈^{7}, fcc-Ru₃₈^{7}, hcp-Ru₅₄^{6}, and fcc-Ru₅₅^{6} nanoparticles. Middle and bottom rows: snapshots and adhesion energies (E_{adh}) of these nanoparticles on the graphene and TiON supports. The cohesion and adhesion energies were calculated with eqs (1) and (2), respectively.

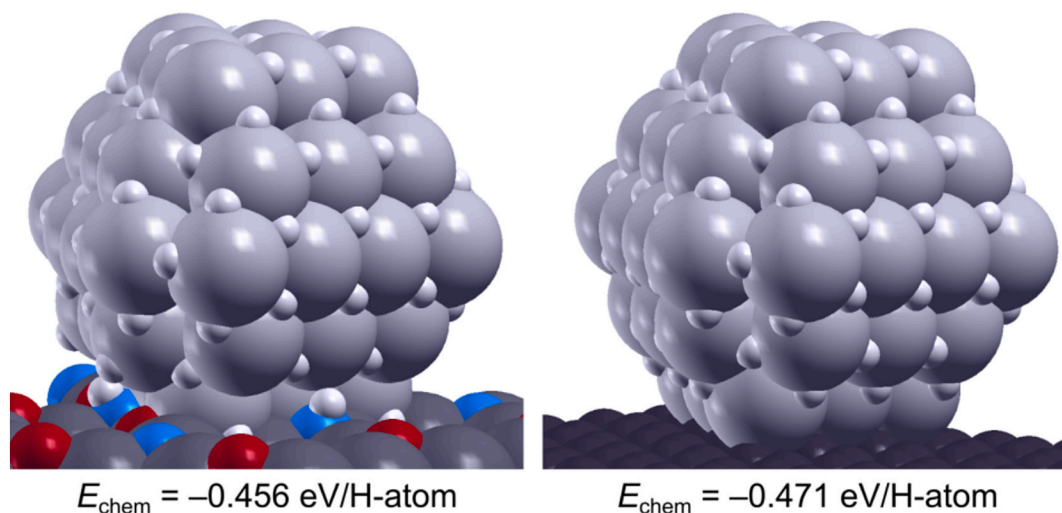


Fig. 10. Optimized structures of the hcp-Ru₅₄(⁶) nanoparticle covered with 76 chemisorbed H atoms and supported on TiON (left) and graphene (right). The average H chemisorption energies are also stated.

nanoparticles tend to weaken their interaction with small adsorbates, provided that the adsorbates bind predominantly covalently [82], which is the case here.

4. Conclusions

This work demonstrates the excellent HER performance of a novel catalyst comprised of Ru nanoparticles supported on TiON dispersed over reduced graphene oxide (Ru/TiON-C). The Ru/TiON-C composite with a low Ru loading of 6 wt% exhibited superior HER activity in alkaline media, surpassing the Ru/C and Pt/C benchmarks, placing itself among the state-of-the-art Ru-based catalysts reported in the literature. At the same time, Ru/TiON-C exhibits stable operation in different degradation tests. Its effective HER performance was attributed to the strong metal–support interaction provided by the TiON support, which was proved by XPS through the shift of the characteristic Ru photoelectron lines, indicating electronic charge redistribution at Ru sites. The existence of MSI was further corroborated by DFT calculations showing a considerably stronger anchoring of Ru nanoparticles and pronounced charge accumulation at the Ru/TiON interface compared to the carbon support. DFT calculations also reveal that the strong MSI results in slightly weaker chemisorbed H atoms at high coverage, which, in turn, should facilitate H₂ formation to some extent, thus enhancing the HER activity of the catalyst. Lastly, the potential presence of the fcc Ru phase—reported in the literature to be catalytically superior to the more stable hcp Ru phase—was investigated using 4D-STEM analysis and DFT calculations, which suggest that the fcc phase may exist. Future work will aim to validate the performance of Ru/TiON-C catalyst under industrially relevant conditions, including integration into membrane electrode assemblies (MEA) and operation at high current densities in two-electrode alkaline water electrolyzer systems. We anticipate that TiON could also be a versatile support for other electrocatalytically active sites and reactions, broadening its potential applications in electrocatalysis.

CRedit authorship contribution statement

M. Smiljanić: Writing – review & editing, Writing – original draft, Visualization, Supervision, Project administration, Investigation, Funding acquisition, Data curation, Conceptualization. **M. Bele:** Investigation, Conceptualization. **L. Pavko:** Methodology, Investigation, Data curation. **A. Hrnjić:** Investigation, Formal analysis. **F. Ruiz-Zepeda:** Methodology, Investigation. **L. Bijelić:** Investigation, Formal analysis,

Data curation. **A.R. Kamšek:** Methodology, Formal analysis. **M. Nuhanović:** Investigation, Formal analysis. **A. Marsel:** Investigation. **L. Gašparić:** Writing – original draft, Visualization, Methodology, Investigation, Formal analysis. **A. Kokalj:** Writing – original draft, Methodology, Formal analysis, Conceptualization. **N. Hodnik:** Writing – original draft, Validation, Supervision, Project administration, Funding acquisition, Conceptualization.

Declaration of competing interest

The authors declare that they have no known competing financial interests or personal relationships that could have appeared to influence the work reported in this paper.

Acknowledgments

This work was financially supported by the Slovenian Research Agency through the research programs/projects P2-0393 and I0-0003 (OE 4), J7-4636, J7-4637, J7-50227, NC-0016, N2-0248, N2-0385, N2-0155, J2-50055, and the grant Artificial Intelligence for Science (GC-0001). The authors also acknowledge financing by the NATO Science for Peace and Security program (Grant G6230) and the European Research Council Starting Grant 123STABLE (Grant agreement ID: 852208). The authors acknowledge partial support from the Republic of Slovenia, the Ministry of Higher Education, Science and Innovation, and the European Union – NextGenerationEU in the framework of the project HyBrED, part of the Slovenian Recovery and Resilience Plan. Views and opinions expressed are however those of the authors only and do not necessarily reflect those of the Republic of Slovenia, the Ministry of Higher Education, the European Union, or the European Commission. Neither the Republic of Slovenia, the Ministry of Higher Education, Science and Innovation, the European Union nor the European Commission can be held responsible for them. A. R. K. acknowledges support from the Milan Lenarčič Foundation and the Janko Jarnik Doctoral Scholarship.

Appendix A. Supplementary data

Supplementary data to this article can be found online at <https://doi.org/10.1016/j.cej.2025.164204>.

Data availability

Data will be made available on request.

References

- [1] J.O.M. Bockris, The hydrogen economy: Its history, *Int J Hydrogen Energy* 38 (2013) 2579–2588, <https://doi.org/10.1016/j.ijhydene.2012.12.026>.
- [2] J.O.M. Bockris, The origin of ideas on a Hydrogen Economy and its solution to the decay of the environment, *Int J Hydrogen Energy* 27 (2002) 731–740, [https://doi.org/10.1016/S0360-3199\(01\)00154-9](https://doi.org/10.1016/S0360-3199(01)00154-9).
- [3] K.T. Møller, T.R. Jensen, E. Akiba, H. wen Li, Hydrogen - A sustainable energy carrier, *Prog. Nat. Sci.: Mater. Int.* 27 (2017) 34–40, <https://doi.org/10.1016/j.pnsc.2016.12.014>.
- [4] M. Carmo, D.L. Fritz, J. Mergel, D. Stolten, A comprehensive review on PEM water electrolysis, *Int J Hydrogen Energy* 38 (2013) 4901–4934, <https://doi.org/10.1016/j.ijhydene.2013.01.151>.
- [5] K. Ayers, N. Danilovic, R. Ouimet, M. Carmo, B. Pivovar, M. Bornstein, Perspectives on low-temperature electrolysis and potential for renewable hydrogen at scale, *Annu Rev Chem Biomol Eng* 10 (2019) 219–239, <https://doi.org/10.1146/annurev-chembioeng-060718-030241>.
- [6] J.N. Hansen, H. Prats, K.K. Toudahl, N. Mørch Secher, K. Chan, J. Kibsgaard, I. Chorkendorff, Is There Anything Better than Pt for HER? *ACS Energy Lett* (2021) 1175–1180, <https://doi.org/10.1021/acsenerylett.1c00246>.
- [7] P. Sabatier, Hydrogenations et deshydrogenations par catalyse, *Ber. Dtsch. Chem. Ges.* 44 (1911) 1984–2001.
- [8] J.K. Nørskov, T. Bligaard, A. Logadottir, J.R. Kitchin, J.G. Chen, S. Pandalov, U. Stimming, Trends in the Exchange Current for Hydrogen Evolution, *J Electrochem Soc* 152 (2005) J23, <https://doi.org/10.1149/1.1856988>.
- [9] W. Sheng, M. Myint, J.G. Chen, Y. Yan, Correlating the hydrogen evolution reaction activity in alkaline electrolytes with the hydrogen binding energy on monometallic surfaces, *Energy Environ Sci* 6 (2013) 1509, <https://doi.org/10.1039/c3ee00045a>.
- [10] P. Quaino, F. Juarez, E. Santos, W. Schmickler, Volcano plots in hydrogen electrocatalysis—uses and abuses, *Beilstein J. Nanotechnol.* 5 (2014) 846–854, <https://doi.org/10.3762/bjnano.5.96>.
- [11] W. Sheng, H.A. Gasteiger, Y. Shao-Horn, Hydrogen Oxidation and Evolution Reaction Kinetics on Platinum: Acid vs Alkaline Electrolytes, *J Electrochem Soc* 157 (2010) B1529, <https://doi.org/10.1149/1.3483106>.
- [12] S.Y. Bae, J. Mahmood, I.Y. Jeon, J.B. Baek, Recent advances in ruthenium-based electrocatalysts for the hydrogen evolution reaction, *Nanoscale Horiz* 5 (2020) 43–56, <https://doi.org/10.1039/c9nh00485h>.
- [13] W. Luo, Y. Wang, C. Cheng, Ru-based electrocatalysts for hydrogen evolution reaction: Recent research advances and perspectives, *Mater. Today Phys.* 15 (2020) 100274, <https://doi.org/10.1016/j.mtphys.2020.100274>.
- [14] Y. Yang, Y. Yu, J. Li, Q. Chen, Y. Du, P. Rao, R. Li, C. Jia, Z. Kang, P. Deng, Y. Shen, X. Tian, Engineering Ruthenium-Based Electrocatalysts for Effective Hydrogen Evolution Reaction, *Nanomicro Lett* 13 (2021), <https://doi.org/10.1007/s40820-021-00679-3>.
- [15] X. Cao, J. Huo, L. Li, J. Qu, Y. Zhao, W. Chen, C. Liu, H. Liu, G. Wang, Recent Advances in Engineered Ru-Based Electrocatalysts for the Hydrogen/Oxygen Conversion Reactions, *Adv Energy Mater* 12 (2022), <https://doi.org/10.1002/aenm.202202119>.
- [16] Q. Wu, M. Luo, J. Han, W. Peng, Y. Zhao, D. Chen, M. Peng, J. Liu, F.M.F. De Groot, Y. Tan, Identifying Electrocatalytic Sites of the Nanoporous Copper-Ruthenium Alloy for Hydrogen Evolution Reaction in Alkaline Electrolyte, *ACS Energy Lett* 5 (2020) 192–199, <https://doi.org/10.1021/acsenerylett.9b02374>.
- [17] S. Zhang, Y. Rui, X. Zhang, R. Sa, F. Zhou, R. Wang, X. Li, Ultrafine cobalt-ruthenium alloy nanoparticles induced by confinement effect for upgrading hydrogen evolution reaction in all-pH range, *Chem. Eng. J.* 417 (2021) 128047, <https://doi.org/10.1016/j.cej.2020.128047>.
- [18] X. Bai, Q.Q. Pang, X. Du, S.S. Yi, S. Zhang, J. Qian, X.Z. Yue, Z.Y. Liu, Integrating RuNi alloy in S-doped defective carbon for efficient hydrogen evolution in both acidic and alkaline media, *Chem. Eng. J.* 417 (2021) 129319, <https://doi.org/10.1016/j.cej.2021.129319>.
- [19] H. Wang, Y. Yang, F.J. Disalvo, H.D. Abrunã, Multifunctional Electrocatalysts: Ru-M (M = Co, Ni, Fe) for Alkaline Fuel Cells and Electrolyzers, *ACS Catal* 10 (2020) 4608–4616, <https://doi.org/10.1021/acscatal.9b05621>.
- [20] Y. Zhao, X. Wang, G. Cheng, W. Luo, Phosphorus-Induced Activation of Ruthenium for Boosting Hydrogen Oxidation and Evolution Electrocatalysis, *ACS Catal* 10 (2020) 11751–11757, <https://doi.org/10.1021/acscatal.0c03148>.
- [21] S. Ye, F. Luo, T. Xu, P. Zhang, H. Shi, S. Qin, J. Wu, C. He, X. Ouyang, Q. Zhang, J. Liu, X. Sun, Boosting the alkaline hydrogen evolution of Ru nanoclusters anchored on B/N-doped graphene by accelerating water dissociation, *Nano Energy* 68 (2020) 104301, <https://doi.org/10.1016/J.NANOEN.2019.104301>.
- [22] Y. Wang, W. Luo, H. Li, C. Cheng, Ultrafine Ru nanoclusters supported on N/S doped macroporous carbon spheres for efficient hydrogen evolution reaction, *Nanoscale Adv* 3 (2021) 5068–5074, <https://doi.org/10.1039/D1NA00424G>.
- [23] Y.-L. Wu, X. Li, Y.-S. Wei, Z. Fu, W. Wei, X.-T. Wu, Q.-L. Zhu, Q. Xu, Y. Wu, X. Li, W. Wei, X. Wu, Q. Zhu, Y. Wei, Q. Xu, Z. Fu, Ordered Macroporous Superstructure of Nitrogen-Doped Nanoporous Carbon Implanted with Ultrafine Ru Nanoclusters for Efficient pH-Universal Hydrogen Evolution Reaction, *Adv. Mater.* 33 (2021) 2006965, <https://doi.org/10.1002/ADMA.202006965>.
- [24] Y. Sun, Z. Xue, Q. Liu, Y. Jia, Y. Li, K. Liu, Y. Lin, M. Liu, G. Li, C.Y. Su, Modulating electronic structure of metal-organic frameworks by introducing atomically dispersed Ru for efficient hydrogen evolution, *Nature Communications* 2021 12:1 12 (2021) 1–8, <https://doi.org/10.1038/s41467-021-21595-5>.
- [25] J. Peng, Y. Chen, K. Wang, Z. Tang, S. Chen, High-performance Ru-based electrocatalyst composed of Ru nanoparticles and Ru single atoms for hydrogen evolution reaction in alkaline solution, *Int J Hydrogen Energy* 45 (2020) 18840–18849, <https://doi.org/10.1016/j.ijhydene.2020.05.064>.
- [26] D. Sui, R. Luo, S. Xie, H. Zhang, T. Ma, H. Sun, T.T. Jia, J. Sun, X. Li, Atomic ruthenium doping in collaboration with oxygen vacancy engineering boosts the hydrogen evolution reaction by optimizing H absorption, *Chem. Eng. J.* 480 (2024) 148007, <https://doi.org/10.1016/j.cej.2023.148007>.
- [27] Y. Zheng, Y. Jiao, Y. Zhu, L.H. Li, Y. Han, Y. Chen, M. Jaroniec, S.Z. Qiao, High Electrocatalytic Hydrogen Evolution Activity of an Anomalous Ruthenium Catalyst, *J Am Chem Soc* 138 (2016) 16174–16181, <https://doi.org/10.1021/jacs.6b11291>.
- [28] K. Gao, Y. Wang, Z. Wang, Z. Zhu, J. Wang, Z. Luo, C. Zhang, X. Huang, H. Zhang, W. Huang, Ru nanodendrites composed of ultrathin fcc/hcp nanoblades for the hydrogen evolution reaction in alkaline solutions, *Chem. Commun.* 54 (2018) 4613–4616, <https://doi.org/10.1039/C8CC01343H>.
- [29] Q. Lu, A.L. Wang, Y. Gong, W. Hao, H. Cheng, J. Chen, B. Li, N. Yang, W. Niu, J. Wang, Y. Yu, X. Zhang, Y. Chen, Z. Fan, X.J. Wu, J. Chen, J. Luo, S. Li, L. Gu, H. Zhang, Crystal phase-based epitaxial growth of hybrid noble metal nanostructures on 4H/fcc Au nanowires, *Nat Chem* 10 (2018) 456–461, <https://doi.org/10.1038/s41557-018-0012-0>.
- [30] L. Moriau, M. Smiljanić, A. Lončar, N. Hodnik, Supported Iridium-based Oxygen Evolution Reaction Electrocatalysts - Recent Developments, *ChemCatChem* 14 (2022) e202200586, <https://doi.org/10.1002/cctc.202200586>.
- [31] S. Jayabal, G. Saranya, D. Geng, L.Y. Lin, X. Meng, Insight into the correlation of Pt-support interactions with electrocatalytic activity and durability in fuel cells, *J Mater Chem A Mater* 8 (2020) 9420–9446, <https://doi.org/10.1039/d0ta01530j>.
- [32] S.J. Tauster, S.C. Fung, R. L. Garten, Strong Metal-Support Interactions, *Metals*, *J Am Chem Soc* 100 (1978) 170–175, <https://doi.org/10.1021/ja00469a029>.
- [33] S.J. Tauster, S.C. Fung, R.T.K. Baker, J.A. Horsley, Strong Interactions in Supported-Metal Catalysts, *Science* 211 (1981) 1121–1125, <https://doi.org/10.1126/science.211.4487.1121>.
- [34] Y. Liu, W.E. Mustain, Evaluation of tungsten carbide as the electrocatalyst support for platinum hydrogen evolution/oxidation catalysts, *Int J Hydrogen Energy* 37 (2012) 8929–8938, <https://doi.org/10.1016/j.ijhydene.2012.03.044>.
- [35] N. Cheng, S. Stambula, D. Wang, M.N. Banis, J. Liu, A. Riese, B. Xiao, R. Li, T. K. Sham, L.M. Liu, G.A. Botton, X. Sun, Platinum single-atom and cluster catalysis of the hydrogen evolution reaction, *Nat Commun* 7 (2016) 1–9, <https://doi.org/10.1038/ncomms13638>.
- [36] J. Zhao, M. Kou, Q. Yuan, Y. Yuan, J. Zhao, Hydrogen Spillover-Bridged Interfacial Water Activation of WCx and Hydrogen Recombination of Ru as Dual Active Sites for Accelerating Electrocatalytic Hydrogen Evolution, *Small* 21 (2024) 2406022, <https://doi.org/10.1002/sml.202406022>.
- [37] Y. Yuan, W. Han, C. Zhang, Q. Sun, Y. Hao, J. Zhao, J. Zhao, X. Zhong, N. Zhang, An insight into the enhanced mechanism of Ru-MoO₂ interfacial chemical bonding for hydrogen evolution reaction in alkaline media, *Nano Res* 16 (2023) 2230–2235, <https://doi.org/10.1007/s12274-022-5013-z>.
- [38] M. Bele, K. Stojanovski, P. Jovanović, L. Moriau, G. Koderman Podboršek, J. Moskon, P. Umek, M. Sluban, G. Dražić, N. Hodnik, M. Gabersček, Towards Stable and Conductive Titanium Oxynitride High-Surface-Area Support for Iridium Nanoparticles as Oxygen Evolution Reaction Electrocatalyst, *ChemCatChem* 11 (2019) 5038–5044, <https://doi.org/10.1002/cctc.201901487>.
- [39] A. Loncar, L. Moriau, K. Stojanovski, F. Ruiz-Zepeda, P. Jovanovic, M. Bele, M. Gabersček, N. Hodnik, Ir/TiO_x/C high-performance oxygen evolution reaction nanocomposite electrocatalysts in acidic media: synthesis, characterization and electrochemical benchmarking protocol, *Journal of Physics: Energy* 2 (2020) 02LT01, <https://doi.org/10.1088/2515-7655/ab69a2>.
- [40] L. Moriau, G. Koderman Podboršek, A.K. Surca, S. Semsari Parpari, M. Šala, U. Petek, M. Bele, P. Jovanović, B. Genorio, N. Hodnik, Enhancing Iridium Nanoparticles' Oxygen Evolution Reaction Activity and Stability by Adjusting the Coverage of Titanium Oxynitride Flakes on Reduced Graphene Oxide Nanoribbons' Support, *Adv Mater Interfaces* 8 (2021) 2100900, <https://doi.org/10.1002/admi.202100900>.
- [41] M. Bele, P. Jovanović, Ž. Marinko, S. Drev, V.S. Šelih, J. Kovač, M. Gabersček, G. Koderman Podboršek, G. Dražić, N. Hodnik, A. Kokalj, L. Suhadolnik, Increasing the Oxygen-Evolution Reaction Performance of Nanotubular Titanium Oxynitride-Supported Ir Nanoparticles by a Strong Metal-Support Interaction, *ACS Catal* 10 (2020) 13688–13700, <https://doi.org/10.1021/acscatal.0c03688>.
- [42] M. Smiljanić, S. Panić, M. Bele, F. Ruiz-Zepeda, L. Pavko, L. Gašparić, A. Kokalj, M. Gabersček, N. Hodnik, Improving the HER Activity and Stability of Pt Nanoparticles by Titanium Oxynitride Support, *ACS Catal* 12 (2022) 13021–13033, <https://doi.org/10.1021/acscatal.2c03214>.
- [43] A. Hrnjić, A.R. Kamšek, L. Bijelić, A. Logar, N. Maselj, M. Smiljanić, J. Trpatec, N. Vovk, L. Pavko, F. Ruiz-Zepeda, M. Bele, P. Jovanović, N. Hodnik, Metal-Support Interaction between Titanium Oxynitride and Pt Nanoparticles Enables Efficient Low-Pt-Loaded High-Performance Electrodes at Relevant Oxygen Reduction Reaction Current Densities, *ACS Catal* (2024) 2473–2486, <https://doi.org/10.1021/ACSCATAL.3C03883>.
- [44] D.C. Marcano, D.V. Kosynkin, J.M. Berlin, A. Sinitskii, Z. Sun, A. Slesarev, L. B. Alemany, W. Lu, J.M. Tour, Improved synthesis of graphene oxide, *ACS Nano* 4 (2010) 4806–4814, <https://doi.org/10.1021/nn1006368>.
- [45] J.F. Vélaz Santa, S. Menart, M. Bele, F. Ruiz-Zepeda, P. Jovanović, V. Jovanovski, M. Šala, M. Smiljanić, N. Hodnik, High-surface-area organic matrix tris(aza) pentacene supported platinum nanostructures as selective electrocatalyst for hydrogen oxidation/evolution reaction and suppressive for oxygen reduction reaction, *Int J Hydrogen Energy* 46 (2021) 25039–25049, <https://doi.org/10.1016/J.IJHYDENE.2021.05.041>.

- [46] C.T. Koch, Determination of core structure periodicity and point defect density along dislocations, Arizona State University, 2002.
- [47] F. Pedregosa FABIANPEDREGOSA, V. Michel, O. Grisel OLIVIERGRISEL, M. Blondel, P. Prettenhofer, R. Weiss, J. Vanderplas, D. Cournapeau, F. Pedregosa, G. Varoquaux, A. Gramfort, B. Thirion, O. Grisel, V. Dubourg, A. Passos, M. Brucher, M. Perrot and Édouardand, and Édouard Duchesnay, Fré. Duchesnay EDOUARDDUCHESNAY, Scikit-learn: Machine Learning in Python Gaël Varoquaux Bertrand Thirion Vincent Dubourg Alexandre Passos PEDREGOSA, VAROQUAUX, GRAMFORT ET AL. Matthieu Perrot, 2011. <http://scikit-learn.sourceforge.net>.
- [48] M. Inaba, A.W. Jensen, G.W. Sievers, M. Escudero-Escribano, A. Zana, M. Arenz, Benchmarking high surface area electrocatalysts in a gas diffusion electrode: Measurement of oxygen reduction activities under realistic conditions, *Energy, Environ Sci* 11 (2018) 988–994, <https://doi.org/10.1039/c8ee00019k>.
- [49] K. Ehelebe, N. Schmitt, G. Sievers, A.W. Jensen, A. Hrnjić, P. Collantes Jiménez, P. Kaiser, M. Geuß, Y.P. Ku, P. Jovanović, K.J.J. Mayrhofer, B. Eitzold, N. Hodnik, M. Escudero-Escribano, M. Arenz, S. Cherevko, Benchmarking Fuel Cell Electrocatalysts Using Gas Diffusion Electrodes: Inter-lab Comparison and Best Practices, *ACS Energy Lett* 7 (2022) 816–826, <https://doi.org/10.1021/acsenenerglett.1c02659>.
- [50] A. Hrnjić, F. Ruiz-Zepeda, M. Gabersček, M. Bele, L. Suhadolnik, N. Hodnik, P. Jovanović, Modified Floating Electrode Apparatus for Advanced Characterization of Oxygen Reduction Reaction Electrocatalysts, *J Electrochem Soc* 167 (2020) 166501, <https://doi.org/10.1149/1945-7111/abc9de>.
- [51] C.L. Green, A. Kucernak, Determination of the platinum and ruthenium surface areas in platinum-ruthenium electrocatalysts by underpotential deposition of copper. 2: Effect of surface composition on activity, *Journal of Physical Chemistry B* 106 (2002) 11446–11456, <https://doi.org/10.1021/jp020859y>.
- [52] P. Giannozzi, O. Andreussi, T. Brumme, O. Bunau, M. Buongiorno Nardelli, M. Calandra, R. Car, C. Cavazzoni, D. Ceresoli, M. Cococcioni, N. Colonna, I. Carnimeo, A. Dal Corso, S. De Gironcoli, P. Delugas, R.A. Distasio, A. Ferretti, A. Floris, G. Fratesi, G. Fugallo, R. Gebauer, U. Gerstmann, F. Giustino, T. Gorni, J. Jia, M. Kawamura, H.Y. Ko, A. Kokalj, E. Küçükbenli, M. Lazzeri, M. Marsili, N. Marzari, F. Mauri, N.L. Nguyen, H.V. Nguyen, A. Otero-De-La-Roz, L. Paulatto, S. Poncè, D. Rocca, R. Sabatini, B. Santra, M. Schlipf, A.P. Seitsonen, A. Smogunov, I. Timrov, T. Thonhauser, P. Umari, N. Vast, X. Wu, S. Baroni, Advanced capabilities for materials modelling with Quantum ESPRESSO, *J. Phys. Condens. Matter* 29 (2017) 465901, <https://doi.org/10.1088/1361-648x/aa8f79>.
- [53] P. Giannozzi, S. Baroni, N. Bonini, M. Calandra, R. Car, C. Cavazzoni, D. Ceresoli, G.L. Chiarotti, M. Cococcioni, I. Dabo, A. Dal Corso, S. De Gironcoli, S. Fabris, G. Fratesi, R. Gebauer, U. Gerstmann, C. Gougoussis, A. Kokalj, M. Lazzeri, L. Martin-Samos, N. Marzari, F. Mauri, R. Mazzarello, S. Paolini, A. Pasquarello, L. Paulatto, C. Sbraccia, S. Scandolo, G. Sclauzero, A.P. Seitsonen, A. Smogunov, P. Umari, R.M. Wentzcovitch, QUANTUM ESPRESSO: A modular and open-source software project for quantum simulations of materials, *J. Phys. Condens. Matter* 21 (2009) 395502, <https://doi.org/10.1088/0953-8984/21/39/395502>.
- [54] J.P. Perdew, K. Burke, M. Ernzerhof, Generalized gradient approximation made simple, *PhysRevLett* 77 (1996) 3865–3868, <https://doi.org/10.1103/PhysRevLett.77.3865>.
- [55] P.E. Blöchl, Projector augmented-wave method, *PhysRevB* 50 (1994) 17953–17979, <https://doi.org/10.1103/PhysRevB.50.17953>.
- [56] A. Dal Corso, Pseudopotentials periodic table: From H to Pu, *Comput Mater Sci* 95 (2014) 337–350, <https://doi.org/10.1016/j.commatsci.2014.07.043>.
- [57] We used PAW potentials from pslibrary, in particular: C.pbe-n-kjpaw_psl.1.0.0.UPF, N.pbe-n-kjpaw_psl.1.0.0.UPF, O.pbe-n-kjpaw_psl.1.0.0.UPF, Ti.pbe-n-kjpaw_psl.1.0.0.UPF, and Ru.pbe-n-kjpaw_psl.1.0.0.UPF., (n.d.).
- [58] M. Methfessel, A.T. Paxton, High-precision sampling for Brillouin-zone integration in metals, *PhysRevB* 40 (1989) 3616–3621, <https://doi.org/10.1103/PhysRevB.40.3616>.
- [59] G. Makov, M.C. Payne, Periodic boundary conditions in ab initio calculations, *PhysRevB* 51 (1995) 4014, <https://doi.org/10.1103/PhysRevB.51.4014>.
- [60] S. Grimme, J. Antony, S. Ehrlich, H. Krieg, A consistent and accurate ab initio parametrization of density functional dispersion correction (DFT-D) for the 94 elements H-Pu, *J. Chem. Phys.* 132 (2010) 154104, <https://doi.org/10.1063/1.3382344>.
- [61] I. Timrov, N. Marzari, M. Cococcioni, Hubbard parameters from density-functional perturbation theory, *PhysRevB* 98 (2018) 1–15, <https://doi.org/10.1103/PhysRevB.98.085127>.
- [62] V.I. Anisimov, J. Zaanen, O.K. Andersen, Band theory and Mott insulators: Hubbard U instead of Stoner I, *PhysRevB* 44 (1991) 943–954, <https://doi.org/10.1103/PhysRevB.44.943>.
- [63] M. Cococcioni, S. De Gironcoli, Linear response approach to the calculation of the effective interaction parameters in the LDA+U method, *Phys Rev B Condens Matter Phys* 71 (2005) 1–16, <https://doi.org/10.1103/PhysRevB.71.035105>.
- [64] M. Li, H. Wang, W. Zhu, W. Li, C. Wang, X. Lu, RuNi Nanoparticles Embedded in N-Doped Carbon Nanofibers as a Robust Bifunctional Catalyst for Efficient Overall Water Splitting, *Adv. Sci.* 7 (2020) 1901833, <https://doi.org/10.1002/advsc.201901833>.
- [65] B.M. Stühmeier, R.J. Schuster, L. Hartmann, S. Selve, H.A. El-Sayed, H. A. Gasteiger, Modification of the Electrochemical Surface Oxide Formation and the Hydrogen Oxidation Activity of Ruthenium by Strong Metal Support Interactions, *J Electrochem Soc* 169 (2022) 034519, <https://doi.org/10.1149/1945-7111/ac58c9>.
- [66] Y. Zhao, X. Wang, Z. Li, P. Zhao, C. Tao, G. Cheng, W. Luo, Enhanced catalytic activity of Ru through N modification toward alkaline hydrogen electrocatalysis, *Chin. Chem. Lett.* 33 (2022) 1065–1069, <https://doi.org/10.1016/j.ccllet.2021.05.038>.
- [67] F. Li, G.F. Han, H.J. Noh, I. Ahmad, I.Y. Jeon, J.B. Baek, Mechanochemically Assisted Synthesis of a Ru Catalyst for Hydrogen Evolution with Performance Superior to Pt in Both Acidic and Alkaline Media, *Adv. Mater.* 30 (2018) 1803676, <https://doi.org/10.1002/adma.201803676>.
- [68] J. Lin, X. Wang, Z. Zhao, D. Chen, R. Liu, Z. Ye, B. Lu, Y. Hou, J. Lu, Design of pH-universal electrocatalysts for hydrogen evolution reaction, *Carbon Energy* (2024) e555.
- [69] J. Mahmood, F. Li, S.M. Jung, M.S. Okyay, I. Ahmad, S.J. Kim, N. Park, H.Y. Jeong, J.B. Baek, An efficient and pH-universal ruthenium-based catalyst for the hydrogen evolution reaction, *Nat Nanotechnol* 12 (2017) 441–446, <https://doi.org/10.1038/nnano.2016.304>.
- [70] H. Yao, X. Wang, K. Li, C. Li, C. Zhang, J. Zhou, Z. Cao, H. Wang, M. Gu, M. Huang, H. Jiang, Strong electronic coupling between ruthenium single atoms and ultrafine nanoclusters enables economical and effective hydrogen production, *Appl Catal B* 312 (2022) 121378, <https://doi.org/10.1016/j.apcatb.2022.121378>.
- [71] K. Wu, K. Sun, S. Liu, W.C. Cheong, Z. Chen, C. Zhang, Y. Pan, Y. Cheng, Z. Zhuang, X. Wei, Y. Wang, L. Zheng, Q. Zhang, D. Wang, Q. Peng, C. Chen, Y. Li, Atomically dispersed Ni–Ru–P interface sites for high-efficiency pH-universal electrocatalysis of hydrogen evolution, *Nano Energy* 80 (2021) 105467, <https://doi.org/10.1016/j.nanoen.2020.105467>.
- [72] Y. Wang, Q. Zhu, T. Xie, Y. Peng, S. Liu, J. Wang, Promoted Alkaline Hydrogen Evolution Reaction Performance of Ru/C by Introducing TiO₂ Nanoparticles, *ChemElectroChem* 7 (2020) 1182–1186, <https://doi.org/10.1002/celec.201902170>.
- [73] D. Li, Y. Liu, Z. Liu, J. Yang, C. Hu, L. Feng, Electrochemical hydrogen evolution reaction efficiently catalyzed by Ru–N coupling in defect-rich Ru/g-C₃N₄nanosheets, *J Mater Chem A Mater* 9 (2021) 15019–15026, <https://doi.org/10.1039/d1ta03809e>.
- [74] L. Tang, J. Yu, Y. Zhang, Z. Tang, Y. Qin, Boosting the hydrogen evolution reaction activity of Ru in alkaline and neutral media by accelerating water dissociation, *RSC Adv* 11 (2021) 6107–6113, <https://doi.org/10.1039/D0RA09515J>.
- [75] Z. Liu, X. Yang, G. Hu, L. Feng, Ru Nanoclusters Coupled on Co/N-Doped Carbon Nanotubes Efficiently Catalyzed the Hydrogen Evolution Reaction, *ACS Sustain Chem Eng* 8 (2020) 9136–9144, <https://doi.org/10.1021/acssuschemeng.0c02636>.
- [76] Y. Luo, X. Luo, G. Wu, Z. Li, G. Wang, B. Jiang, Y. Hu, T. Chao, H. Ju, J. Zhu, Z. Zhuang, Y. Wu, X. Hong, Y. Li, Mesoporous Pd@Ru Core-Shell Nanorods for Hydrogen Evolution Reaction in Alkaline Solution, *ACS Appl Mater Interfaces* 10 (2018) 34147–34152, <https://doi.org/10.1021/acsami.8b09988>.
- [77] A. Hartig-Weiss, M.F. Tovini, H.A. Gasteiger, H.A. El-Sayed, OER catalyst durability tests using the rotating disk electrode technique: The reason why this leads to erroneous conclusions, *ACS Appl Energy Mater* 3 (2020) 10323–10327, https://doi.org/10.1021/ACSAEM.0C01944/ASSET/IMAGES/LARGE/AEOC01944_0002.JPEG.
- [78] T. Lazaridis, B.M. Stühmeier, H.A. Gasteiger, H.A. El-Sayed, Capabilities and limitations of rotating disk electrodes versus membrane electrode assemblies in the investigation of electrocatalysts, *Nat Catal* 5 (2022) 363–373, <https://doi.org/10.1038/s41929-022-00776-5>.
- [79] L. Lin, Z. Sun, M. Yuan, J. He, R. Long, H. Li, C. Nan, G. Sun, S. Ma, Significant enhancement of the performance of hydrogen evolution reaction through shape-controlled synthesis of hierarchical dendrite-like platinum, *J Mater Chem A Mater* 6 (2018) 8068–8077, <https://doi.org/10.1039/C8TA00993G>.
- [80] S. Cherevko, S. Geiger, O. Kasian, N. Kulyk, J.P. Grote, A. Sava, B.R. Shrestha, S. Merzlikin, B. Breitbach, A. Ludwig, K.J.J. Mayrhofer, Oxygen and hydrogen evolution reactions on Ru, RuO₂, Ir, and IrO₂ thin film electrodes in acidic and alkaline electrolytes: A comparative study on activity and stability, *Catal Today* 262 (2016) 170–180, <https://doi.org/10.1016/j.cattod.2015.08.014>.
- [81] U. Joshi, S. Malkhandi, Y. Ren, T.L. Tan, S.Y. Chiam, B.S. Yeo, Ruthenium-Tungsten Composite Catalyst for the Efficient and Contamination-Resistant Electrochemical Evolution of Hydrogen, *ACS Appl Mater Interfaces* 10 (2018) 6354–6360, <https://doi.org/10.1021/acsami.7b17970>.
- [82] C.T. Campbell, J.R.V. Sellers, Anchored metal nanoparticles: Effects of support and size on their energy, sintering resistance and reactivity, *Faraday Discuss* 162 (2013) 9–30, <https://doi.org/10.1039/c3fd00094j>.